

The relative influence of H2O and CO2 on the primitive surface conditions and evolution of rocky planets

Arnaud Salvador, Hélène Massol, Anne Davaille, Emmanuel Marcq, Philippe Sarda, Eric Chassefière

▶ **To cite this version:**

Arnaud Salvador, Hélène Massol, Anne Davaille, Emmanuel Marcq, Philippe Sarda, et al.. The relative influence of H2O and CO2 on the primitive surface conditions and evolution of rocky planets. Journal of Geophysical Research. Planets, 2017, 122 (7), pp.1458-1486. 10.1002/2017JE005286 . insu-01540209

HAL Id: insu-01540209
https://insu.hal.science/insu-01540209

Submitted on 18 Nov 2020

HAL is a multi-disciplinary open access archive for the deposit and dissemination of scientific research documents, whether they are published or not. The documents may come from teaching and research institutions in France or abroad, or from public or private research centers.

L'archive ouverte pluridisciplinaire **HAL**, est destinée au dépôt et à la diffusion de documents scientifiques de niveau recherche, publiés ou non, émanant des établissements d'enseignement et de recherche français ou étrangers, des laboratoires publics ou privés.

AGU PUBLICATIONS

JGR

Journal of Geophysical Research: Planets

RESEARCH ARTICLE
10.1002/2017JE005286

Key Points:
- Magma ocean and atmospheric coupled modeling during the first million years
- Critical distance for water ocean formation obeys simple scaling laws
- Venus might have condensed a water ocean during its history

Correspondence to:
A. Salvador,
arnaud.salvador@u-psud.fr

Citation:
Salvador, A., H. Massol, A. Davaille, E. Marcq, P. Sarda, and E. Chassefière (2017), The relative influence of H_2O and CO_2 on the primitive surface conditions and evolution of rocky planets, *J. Geophys. Res. Planets*, *122*, 1458–1486, doi:10.1002/2017JE005286.

Received 14 FEB 2017
Accepted 12 JUN 2017
Accepted article online 15 JUN 2017
Published online 18 JUL 2017

©2017. American Geophysical Union. All Rights Reserved.

The relative influence of H_2O and CO_2 on the primitive surface conditions and evolution of rocky planets

A. Salvador[1,2], H. Massol[2], A. Davaille[1], E. Marcq[3], P. Sarda[2], and E. Chassefière[2]

[1]FAST, CNRS, Univ. Paris-Sud, Université Paris-Saclay, Orsay, France, [2]GEOPS, CNRS, Univ. Paris-Sud, Université Paris-Saclay, Orsay, France, [3]LATMOS/IPSL, UVSQ, Université Paris-Saclay, Guyancourt, France

Abstract How the volatile content influences the primordial surface conditions of terrestrial planets and, thus, their future geodynamic evolution is an important question to answer. We simulate the secular convective cooling of a 1-D magma ocean (MO) in interaction with its outgassed atmosphere. The heat transfer in the atmosphere is computed either using the grey approximation or using a *k*-correlated method. We vary the initial CO_2 and H_2O contents (respectively from 0.1×10^{-2} to 14×10^{-2} wt % and from 0.03 to 1.4 times the Earth Ocean current mass) and the solar distance—from 0.63 to 1.30 AU. A first rapid cooling stage, where efficient MO cooling and degassing take place, producing the atmosphere, is followed by a second quasi steady state where the heat flux balance is dominated by the solar flux. The end of the rapid cooling stage (ERCS) is reached when the mantle heat flux becomes negligible compared to the absorbed solar flux. The resulting surface conditions at ERCS, including water ocean's formation, strongly depend both on the initial volatile content and solar distance D. For $D > D_C$, the "critical distance," the volatile content controls water condensation and a new scaling law is derived for the water condensation limit. Although today's Venus is located beyond D_C due to its high albedo, its high CO_2/H_2O ratio prevents any water ocean formation. Depending on the formation time of its cloud cover and resulting albedo, only 0.3 Earth ocean mass might be sufficient to form a water ocean on early Venus.

Plain Language Summary Early in their history, Earth-like planets are impacted by small rocky bodies, and the energy brought by the impactors heats the planet. Giant impactors can even remove the atmosphere and melt a large and deep fraction of the planet, leading to the formation of an "ocean" of molten rocks. From this initial stage, cooling and solidification proceed, expelling volatiles to rebuild an atmosphere. Varying the initial CO_2 and H_2O contents for planets located at different distances from the star, we study their influence on the planet evolution and on the surface temperature and pressure. These will condition the formation of a water ocean and the tectonic regime of the solid-state planet. From our calculations, we derived simple relations to forecast water ocean formation. They suggest that a water ocean might have formed on Venus early in its history.

1. Introduction

Based on theory and observations, it is generally accepted that the mantle of terrestrial planets has been partially or totally molten at the end of the accretion process, behaving rheologically as a liquid during the first evolution stages of these bodies [*Wood et al.*, 1970; *Safronov*, 1978; *Hostetler and Drake*, 1980]. It is thus likely that terrestrial planets experienced, early in their history, a magma ocean stage where rapid cooling takes place [*Matsui and Abe*, 1986, see also *Elkins-Tanton*, 2012; *Solomatov*, 2015; *Massol et al.*, 2016 for reviews]. The heating sources involved, and especially the heat conversion from impacts, are not particularly specific to the Earth, since the mechanisms of planetesimal and planet building are common to all planetary systems. However, after a rapid cooling stage, the heat flux released from the interior will depend on the convective patterns and tectonic style of the planet. Recent literature emphasizes how important it is to couple the different planetary envelopes from the core to the atmosphere, in order to understand the diversity of tectonic regimes [*Foley et al.*, 2014; *Foley and Driscoll*, 2016; *Gillmann and Tackley*, 2014; *Gillmann et al.*, 2016]. Indeed, an important number of feedbacks, not always well understood, arise from the interaction between the different envelopes which can lead to surface conditions and evolutionary scenarios totally different

(see *Foley and Driscoll* [2016] for a review). However, most of these models postulate rather than calculate surface conditions at the end of the rapid cooling stage (hereafter "ERCS") to infer the subsequent geodynamic evolution.

Apart from setting the initial state for subsequent geodynamic regimes, another important motivation to develop predictive models of *P-T* surface conditions at ERCS is to forecast surface water condensation. The latter strongly depends on the star-planet distance. Historically, habitable zones (HZ) are defined as the range of orbits around a star within which a planetary surface can maintain liquid water [e.g., *Hart*, 1979; *Kasting et al.*, 1993]. The inner edge of this zone is located where runaway greenhouse conditions prevent the existence of liquid water at the surface because of a too high surface temperature. This inner limit depends on the volatile content of the atmosphere as well as on the atmospheric heat transfer model used (for a review see *Lammer et al.* [2009]). Depending on the models, the inner limit for our solar system ranges between 0.75 and 0.99 AU [*Abe et al.*, 2011; *Kopparapu et al.*, 2013]. Following the detection of potentially habitable exoplanets located in the habitable zone of their star, recent literature has improved and complexified radiative-convective atmospheric models to predict more precisely the HZ limits. For instance, *Kopparapu et al.* [2013] recent 1-D radiative-convective, cloud-free, climate model places the inner and outer edges at respectively 0.99 and 1.7 AU for our solar system. These limits may vary with planetary mass, type of star [*Kopparapu*, 2013; *Kopparapu et al.*, 2014], or with planetary albedo, especially for CO_2-rich atmospheres [*Selsis et al.*, 2007].

In these models, planetary atmospheres are usually considered as H_2O-dominated with a maximum of 150 bar of CO_2 [*Abe et al.*, 2011]. Nevertheless, considering the Earth's volatiles budget, CO_2 appears to be the second most abundant component [*Poldervaart*, 1955]. Inventories estimate that 60 bar of CO_2 can be trapped in carbonate rocks [*Ronov and Yaroshevsky*, 1969; *Holland*, 1978]. Other stellar systems with different scenarios of planet formation may also lead to more volatile-rich planets, such as the Gliese 581 system [*Selsis et al.*, 2007]. Hence, it seems that more CO_2-rich atmospheres might be plausible. Furthermore, measurements on oceanic basalts show that total terrestrial carbon might be very high, as high as thousands of ppm CO_2 [*Sarda and Graham*, 1990; *Pineau and Javoy*, 1994; *Cartigny et al.*, 2008; *Helo et al.*, 2011]. Of course, large uncertainties remain depending on the formation processes and origins of volatile elements [*Raymond et al.*, 2007; *Morbidelli et al.*, 2012; *Marty*, 2012]. For example, atmospheric water content of Earth-mass planets may range between 0.3 and 1000 water oceans depending on accretion duration and planet position within the protoplanetary disk [*Ikoma and Genda*, 2006; *Elkins-Tanton*, 2011; *Lammer et al.*, 2014]. Note that H_2O dominates the outgoing thermal IR spectrum. Thus, CO_2 and reduced species in the case of reducing atmospheres [*Hashimoto et al.*, 2007; *Schaefer and Fegley*, 2010] would play the similar role of noncondensable components with some IR opacity [*Marcq*, 2012].

Upon accretion, Mercury, Venus, the Earth, Mars, and the Moon were probably not so far from each other in terms of volatile content. Then, the bodies evolved differently to give the current diversity of terrestrial planets. To predict surface conditions at ERCS, we conducted a numerical study of the thermal evolution of a magma ocean in interaction with the atmosphere (based on *Lebrun et al.* [2013] and the recently updated *Marcq et al.* [2017] radiative-convective code from *Marcq* [2012]). We investigate the relative influence of the MO initial volatile content for two species, H_2O and CO_2, combined with the solar distance, using two different atmospheric radiative-convective heat transfer models: grey or nongrey.

Section 2 presents the numerical model, focusing on the updates made since *Lebrun et al.* [2013]. It allows to solve simultaneously for (i) the convective thermal evolution of the magma ocean, (ii) the radiative-convective heat transfer within the outgassed atmosphere, and (iii) the interaction between these two reservoirs through the heat and mass balance at the planet surface. Section 3 discusses the main variables (*P-T*, atmospheric composition) evolution during MO cooling, and which conditions allow for water condensation on the surface at the end of the rapid cooling stage (ERCS). From this systematic study, scaling laws for the HZ inner edge location are derived as a function of volatile content and distance to the star and discussed in section 4. Section 5 then investigates how the differences between the Earth and Venus might have arisen.

2. Method

We summarize below the main ingredients of our model, which constitutes an update of *Lebrun et al.* [2013] and detail the changes compared to this previous model.

2.1. Magma Ocean

We assume that the mantle has been strongly warmed up due to the energy brought by the impacts occurring during the accretion. Secular cooling (SC) of the MO is then controlled by the conservation of energy following [e.g., *Abe*, 1997; *Solomatov*, 2000; *Lebrun et al.*, 2013]:

$$\mathrm{SC} = \int_{R_b}^{R_p} \rho C_p \frac{\mathrm{d}T(r)}{\mathrm{d}t} r^2 \mathrm{d}r = R_p^2 F_{\mathrm{conv}} + R_b^2 F_b + H_{\mathrm{int}} + H_{\mathrm{sol}}, \quad (1)$$

where ρ is the averaged density of melt and solid, C_p the specific heat, T the radial temperature, and r the planetary radius variable. t is time. R_p and R_b stand respectively for the planetocentric altitude of the spherical planet surface and that of the base of the magma ocean, from which the heat fluxes F_{conv} and F_b are respectively emitted. H_{int} corresponds to the internal heat from radioactive elements and H_{sol} to the latent heat of solidification. We do not take into account F_b and H_{sol} which are negligible compared to F_{conv}.

2.1.1. Initial State

An initial potential temperature T_{pot} of 4000 K is consistent with both post-major-impact conditions [e.g., *Canup*, 2008; *Tonks and Melosh*, 1993] and theoretical thermodynamical calculations [e.g., *Stixrude et al.*, 2009]. This supports the idea of a totally molten mantle during the accretion phase. We shall therefore consider an Earth-like planet with a mantle which is initially completely molten.

The location of the first solids within the mantle then depends on their respective density compared to the liquids, and the curvature of their melting curves compared to the mantle's adiabat. Recent petrological experiments show that they vary significantly depending on the chemical composition of the starting material: chondritic [*Andrault et al.*, 2011], fertile peridotite [*Fiquet et al.*, 2010], mid-ocean ridge basalt [*Andrault et al.*, 2014], olivine system [*Nomura et al.*, 2011], and pyrolitic material [*Tateno et al.*, 2014]. The two last studies report strong Fe enrichment in the melt, which would therefore be denser than the solids. This would support the idea of a basal magma ocean [*Labrosse et al.*, 2007]. On the other hand, thermodynamical calculations [*Boukaré et al.*, 2015] obtain slightly different melting curves. This model of the solid-liquid equilibrium in the MgO-FeO-SiO_2 system (Al and Ca not being present in the melt) confirms that the melt is lighter than the solid of same composition for all mantle conditions. But it also shows that for the *P-T* conditions of the lowermost mantle, crystallization may lead to the formation of solids lighter than the surrounding melt (as they are more Mg-rich and less Fe-rich). This would favor again the formation of a basal magma ocean. However, *Andrault et al.* [2012] point out that the presence or absence of Al can also influence the density inversion.

Thus, as the formation of an individual magma ocean at the base of the mantle is still debated, we consider the simpler case of a magma ocean of chondritic composition (such as *Andrault et al.* [2011]) crystallizing from bottom-up (Figures 1 and 2). We consider the details of neither petrological nor geochemical processes even if they might be important to generate stratification in a planet [*Elkins-Tanton*, 2008; *Maurice et al.*, 2017]. Unless these processes create an early light stagnant lid on the surface during the magma ocean stage, they should not affect significantly the surface heat flux [*Solomatov*, 2007; *Jaupart and Mareschal*, 2011], which is one of the main parameter controlling the surface conditions we are interested in.

2.1.2. Magma Ocean's Viscosity

Initially, the MO is in a totally molten state. During solidification, the melt fraction ϕ ranges respectively from 1 (totally molten) to 0 (totally solid) and is defined following *Abe* [1997]:

$$\phi = \frac{T - T_{\mathrm{sol}}}{T_{\mathrm{liq}} - T_{\mathrm{sol}}} \quad (2)$$

where T_{sol} and T_{liq} are respectively the solidus and liquidus temperatures (see Figure 2). As solidification proceeds, the liquid fraction ϕ decreases and the connectivity of the crystalline network becomes important, leading to an abrupt viscosity increase. The viscosity of the MO fluid therefore strongly depends on its temperature and crystal content [e.g., *Solomatov*, 2007].

When $\phi > \phi_c$, where ϕ_c is the critical melt fraction (typically $\approx$0.4), the viscosity of the magma is the viscosity of a magmatic liquid containing crystals [*Roscoe*, 1952]:

$$\eta = \frac{\eta_l}{\left(1 - \frac{(1-\phi)}{(1-\phi_c)}\right)^{2.5}}, \quad (3)$$

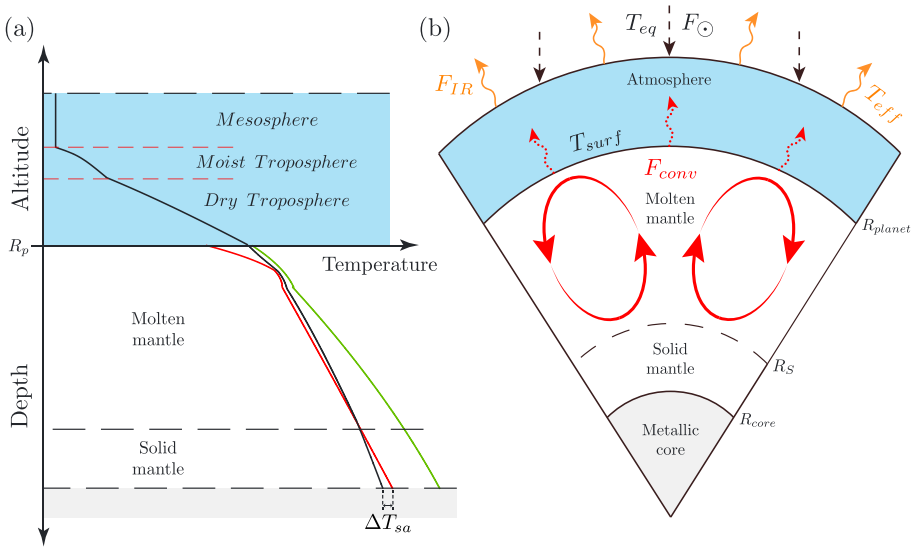


Figure 1. (a) Temperature profile, solidus, and liquidus (black, red, and green curves, respectively); ΔT_{sa} stands for superadiabatic temperature difference. (b) Schematic cross section of a planet in the magma ocean stage surrounded by its atmosphere. F_{conv} stands for the convective heat flux out of the magma ocean (red dotted arrows); $F_\odot$ is the absorbed incoming stellar flux (black dashed arrows). These two incoming heat fluxes balance the outgoing infrared flux at the top of the atmosphere, F_{IR} (orange plain arrows). See text for the definition and expression of the different heat fluxes (sections 2.1.3 and 2.2).

with

$$\eta_l = A_a \exp\left(\frac{B_a}{T_{pot} - 1000}\right) \tag{4}$$

the viscosity of the magmatic liquid derived from the Vogel-Fulcher-Tammann equation, where $A_a = 0.00024$ Pa s and $B_a = 4600$ K [*Karki and Stixrude*, 2010].

When $\phi < \phi_c$, the viscosity of the magma is controlled by the viscosity of the solid particles [*Kelemen et al.*, 1997; *Mei et al.*, 2002; *Solomatov*, 2007]:

$$\eta = \eta_s \exp(-\alpha_\eta \phi) \tag{5}$$

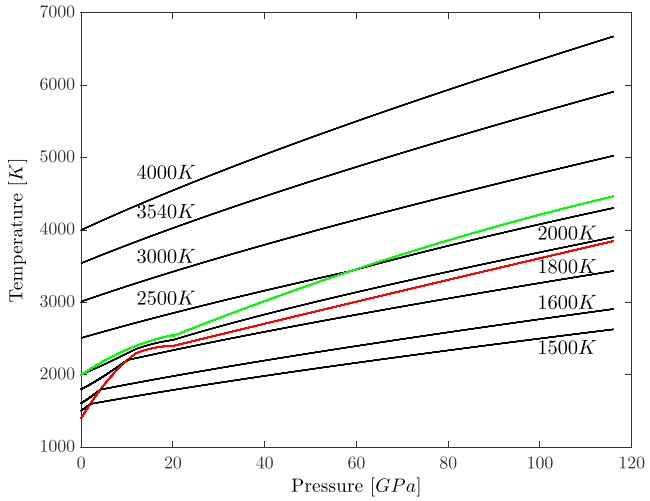


Figure 2. Solidus (red line) and liquidus (green line) for a chondritic mantle, redrawn after *Andrault et al.* [2011]. Adiabatic temperature profiles (black lines) shown at different cooling stages. The adiabats first intersect the solidus deeper, which causes solidification to occur from the base of the mantle toward the surface. Parameters used are given in Table 2.

Table 1. Constant Parameters Used in This Study

Parameter Description	Notation	Value	Unit
Planetary Constants			
Planetary radius	R_p	6378	km
Radius of the base of the MO	R_b	3493	km
Initial depth of the MO	$(R_p - R_b)$	2885	km
Mean density of the planet	ρ_p	5515	kg m^{-3}
Melt density	ρ_m	4000	kg m^{-3}
Solid density	ρ_s	4200	kg m^{-3}
Averaged density of melt and solid	ρ	4100	kg m^{-3}
Mass of the planet	M_p	5.994×10^{24}	kg
Gravitational acceleration	g	9.81	m s^{-2}
Averaged solar constant	$\mathcal{F}_0'$	243	W m^{-2}
Thermal diffusivity	κ	10^{-6}	m^2 s^{-1}
Thermal expansion coefficient	α_T	3×10^{-5}	none
Specific heat	C_p	1000	J kg^{-1} K^{-1}
Pattern of convection, coefficient	C_0	0.089	none
Regime of convection, coefficient	n_{liq}	1/3	none
	n_{sol}	1/3	none
Stefan-Boltzmann constant	σ	5.67×10^{-8}	W m^{-2} K^{-4}
Bolometric albedo	α	0.2	none
H_2O mass absorption coefficient (grey)	k_{H_2O}	10^{-2}	m^2 kg^{-1}
CO_2 mass absorption coefficient (grey)	k_{CO_2}	10^{-4}	m^2 kg^{-1}
Viscosity-Related Parameters			
Coefficient in melt fraction-dependent viscosity	α_η	26	none
Shear modulus	μ	80	GPa
Preexponential factor	A	5.3×10^{15}	none
Grain size	h	10^{-3}	m
Burger vector length	b	0.5	nm
Activation energy	E	240	kJ mol^{-1}
Classic critical liquid fraction	ϕ_c	0.4	none
Distribution Coefficients for the Volatiles			
H_2O partition coefficient (Perovskite)	$k_{H_2O_{perov}}$	10^{-4}	none
CO_2 partition coefficient (Perovskite)	$k_{CO_{2perov}}$	5×10^{-4}	none
H_2O partition coefficient (Lherzolite)	$k_{H_2O_{lherz}}$	1.1×10^{-2}	none
CO_2 partition coefficient (Lherzolite)	$k_{CO_{2lherz}}$	2.1×10^{-3}	none

with, after *Karato and Wu* [1993],

$$\eta_s = \frac{\mu}{2A}\left(\frac{h}{b}\right)^{2.5} \exp\left(\frac{E + PV}{RT_{\mathrm{pot}}}\right), \tag{6}$$

where P, V are pressure and volume, R is the perfect gas constant, and other parameters are defined in Table 1.

Recent experimental data [*Takei and Holtzman*, 2009] suggest that for very small melt volume fractions ($\phi < 0.01$), viscosity is lower than expected due to melt contiguity and that the classical rheology transition between equations (3) and (5) is too abrupt to be realistic. In order to model this transition, we interpolate with a third-order polynomial between the liquid state (equation (3)), and the solid state (equation (5)) (see Figure 3).

This interpolation gives a continuous viscosity law for the explored temperature range and smoothes the rheology transition between the vigorously convective liquid-state and the solid-like mantle (Figure 1). It also

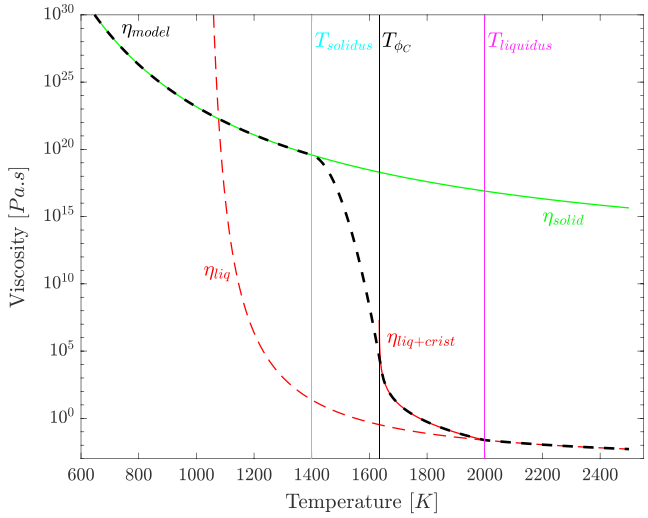


Figure 3. Viscosity laws as a function of temperature for different rheologies. The black dashed line represents the viscosity law of our model. Red dashed line indicates the viscosity of a totally liquid magma: $\phi = 1$ and $T \geq T_{\text{liq}}$ (equation (4) after *Karki and Stixrude* [2010]); red line shows the viscosity of a partially molten magma: $\phi_c < \phi < 1$ and $T_{\phi_c} < T < T_{\text{liq}}$ (equation (3) after *Roscoe* [1952]); and green line stands for the viscosity of solid materials: $\phi = 0$ and $T \leq T_{\text{sol}}$ (equation (5) after *Kelemen et al.* [1997]). We used an analytic expression for the mush stage, between T_{ϕ_c} and T_{sol} ($0 < \phi < \phi_c$): $\eta_{\text{analytic}} = \eta_s \times \exp\left(a_{\text{mush}} \times \phi_{\text{int}}^3 + b_{\text{mush}} \times \phi_{\text{int}}^2\right)$.

allows the refinement of the time steps at that critical stage and consequently, better constraints on pressures and temperatures. Compared to *Lebrun et al.* [2013], this new treatment of the rheology produces a smoother transition from a liquid MO to a solid-state mantle but does not change drastically the dynamics (Figure A1).

2.1.3. Magma Ocean's Thermal Regime

In equation (1), the surface heat flux extracted from the mantle F_{conv} depends on the intensity of convection in the MO and writes

$$F_{\text{conv}} = C_0 k \frac{T_{\text{pot}} - T_{\text{surf}}}{H} Ra(H, T_{\text{pot}} - T_{\text{surf}})^n, \tag{7}$$

where the Rayleigh number associated with temperature difference ΔT over a mantle thickness H is

$$Ra(H, \Delta T) = \frac{\alpha_T g \Delta T H^3}{\kappa \nu}, \tag{8}$$

where κ is the thermal diffusivity, $k = \kappa \rho C_p$ is the thermal conductivity, α_T is the thermal expansion coefficient, $\nu = \eta/\rho$ is the kinematic viscosity, and η is the dynamic viscosity. C_0 is a constant which depends on the pattern of convection (Table 1) [e.g., *Siggia*, 1994]. The value of the exponent n is still debated for the very high Ra of a MO but is usually taken as $n = 1/3$, which implies that the surface heat transfer (F_{conv}) is a local process and is independent of the MO depth [e.g., *Solomatov*, 2015].

As solidification proceeds, zones of different rheology develop, and the convective time scales within each zone are expected to be different given their respective viscosity. This has no influence on F_{conv} as discussed above, but it will affect the secular cooling defined in equation (1), and therefore the MO temporal evolution. If we assume that as soon as the local geotherm reaches the solidus, it stays locked to it, then the mantle secular cooling SC in equation (1) is reduced to the integration of the temperature profile over the molten upper layer only (i.e., between the solidification front and the surface). This implies that the growing solid layer underneath does not become unstable and does not overturn before the whole molten layer has solidified. It gives a minimum estimate of the MO solidification time. However, for Earth-sized planets, scaling analysis and numerical simulations suggest that convection has the time to develop in the solid layer before the whole MO solidification (see discussion in Appendix B). This tends to homogenize the temperature in the whole mantle. Moreover, rotation and differentiation could also enhance mantle thermal homogenization [e.g., *Moeller and Hansen*, 2013; *Maas and Hansen*, 2015; *Maurice et al.*, 2017]. That is why we have chosen to approximate these 3-D complex processes by reducing the secular cooling in equation (1) to the integration of the adiabatic temperature profile $T(r)$ over the whole mantle. This constitutes one of the limitations of our 1-D model.

2.2. Mantle-Atmosphere Coupling

The internal model is coupled with a 1-D radiative-convective atmospheric thermal evolution model through both heat flux balance and volatile balance. It has been developed by *Marcq* [2012], and we use here its most recent update [*Marcq et al.*, 2017]. It is generally assumed that during the early history of terrestrial planets, the primordial atmosphere was lost [e.g., *Cameron*, 1983; *Ahrens*, 1993]. Then, degassing of planetary interiors results in the formation of secondary atmospheres [e.g., *Rubey*, 1951; *Holland*, 1962] that are assumed to be compositionally dominated by H_2O and CO_2. Most likely, this outgassing mainly occurs during MO solidification [e.g., *Elkins-Tanton*, 2008; *Lebrun et al.*, 2013; *Hamano et al.*, 2013] (see *Massol et al.* [2016] for a review). Here we consider that the atmosphere is formed through MO degassing, following a single giant impact, and that at early times, no atmosphere is present.

Most of our calculations are based on the grey version of the atmospheric model, which numerically runs much faster and allows an easier understanding of the system. Nevertheless, section 4.1 also presents calculations carried out with a nongrey atmosphere to discuss the effect of the radiative transfer treatment. The grey model is radiative-convective but assumes constant mass absorption coefficients for H_2O and CO_2 over the spectral range from 0 to 10^4 cm^{-1}. It provides cruder estimates of the resulting heat flux going out of the atmosphere. The nongrey approximation uses wavelength-dependent mass absorption coefficients for both species, from high-resolution spectra computed by KSPECTRUM [*Eymet et al.*, 2016]; (see section 4.1 and *Marcq et al.* [2017] for more details).

Figure 1 summarizes the heat sources for the atmosphere:

1. At the top of the atmosphere, the absorbed solar flux $F_\odot$, defined as

$$F_\odot = \sigma T_{eq}^4 = (1-\alpha) \times \frac{\mathcal{F}_0'}{D^2}, \tag{9}$$

   where σ is the Stefan-Boltzmann constant, T_{eq} the equilibrium temperature (depending only on the absorbed solar flux), α the bolometric albedo ($\alpha = 0.2$ in our calculations), D the planet-star distance (in AU), $\mathcal{F}_0'$ the averaged solar constant over the surface of a planet for a young sun-like star ($\mathcal{F}_0' = \mathcal{F}_0/4$) and $\mathcal{F}_0$ the solar constant. Starting from an initial flux $\mathcal{F}_{0,\,t=0}$ around 70% of the present-day value [*Ezer and Cameron*, 1965], the solar constant increases with time to reach the present-day value as

$$\mathcal{F}_{0,\,t} = \mathcal{F}_{0,\,t=0} \left[1 + 0.4\left(1 - \frac{t}{t_0}\right)\right]^{-1}, \tag{10}$$

   where t is the time, t_0 the age of the solar system (see equation (1) in *Gough* [1981] and Table 2 in *Bahcall et al.* [2001]) and with an early solar constant equal to 972 W m^{-2}, corresponding to an averaged solar constant over the surface of the planet $\mathcal{F}_0' = 243$ W m^{-2}. At the surface, the resulting radiative heat flux depends on the chemical composition of the atmosphere and especially on the greenhouse gases concentrations.
2. At the planetary surface, the internal heat flux F_{conv}, resulting from the initial heat gained during accretion. This flux strongly decreases during MO cooling and finally becomes even lower than the absorbed solar flux $F_\odot$.

As described in *Lebrun et al.* [2013], the outgoing radiative flux F_{IR} escaping into space from the top of the atmosphere must balance the incoming fluxes $F_\odot$ and F_{conv} (see Figure 1 for schematic view).

Figure 4 shows two typical atmospheric temperature profiles. Based on atmospheric pressures and composition, the absorption, emission, and diffusion (i.e., opacity) coefficients of each atmospheric infinitesimal layer in the radiative part of the atmosphere (mesosphere) are calculated. This atmospheric layer is isothermal (Figure 4). When the optical depth of the atmosphere $\langle\tau\rangle_\lambda = 2/3$, i.e., the altitude where effective emission to space and attenuation of sunlight occurs, is reached, convective motions control heat transfer of the underlying layer(s). If the water vapor saturation is reached, condensation occurs, and the moist troposphere has a different convective lapse rate $(\partial T/\partial P)_S$ than the dry troposphere due to latent heat release from condensation (Figure 4a). If the moist troposphere extends to the surface (saturation pressure reached at the surface), any water in excess of 100% saturation is assumed to condense and form a water ocean (Figure 4b) [*Marcq et al.*, 2017]. Note that moist greenhouse atmospheres have no unsaturated troposphere compared to fully runaway greenhouse atmospheres where water oceans have been evaporated [*Kasting*, 1988].

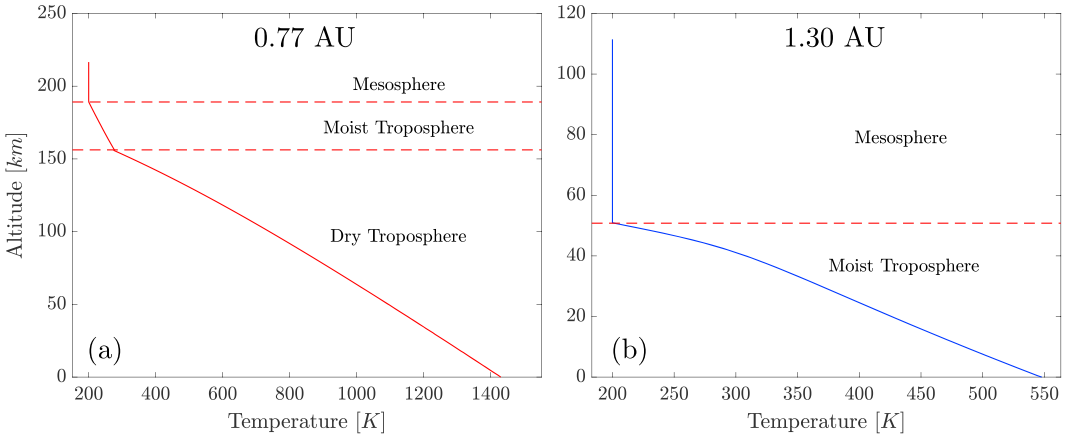


Figure 4. Atmospheric temperature profiles for planets located at (a) 0.77 (red) and (b) 1.30 AU (blue) at the end of the rapid cooling stage. At 1.30 AU, the moist troposphere reaches the surface and formation of a 480 m deep water ocean occurs. Parameters used for the calculations are given in Table 2.

A global emissivity of the atmosphere ε is calculated by the atmospheric model as a function of T_{surf}, P_{H_2O} and P_{CO_2}. The resulting F_{IR} flux (also known as Outgoing Long-wave Radiation, "OLR") quantifies the cooling of the planet. It depends on the atmospheric composition, evolving as magma ocean degasses. After several iterations, we obtain a surface temperature resulting from the flux equilibrium $F_{conv} + F_{\odot} = F_{IR}$ for the atmospheric composition.

Volatile exchanges between the two reservoirs are modeled using the same parametrization as *Lebrun et al.* [2013], in which we assume that the time for a liquid parcel within the convective MO to reach the surface is shorter than the global cooling time. It implies that the dissolved volatiles in the MO are in equilibrium with the atmospheric pressure at each time step (see Appendix C for details and used solubility laws).

We vary the initial volatiles concentration as much as possible within the limit of our model, in particular to keep a realistic atmospheric height compared to the planetary radius, limited by our plane-parallel approximation. For H_2O, we test initial amounts (hereafter $[H_2O]_{t0}$) varying from 0.03 to 1.24 times the current ocean mass

Table 2. Physical Variables Used in This Study

Figure	$X_{0_{H_2O}}$ (10^{-2}wt %)	$X_{0_{H_2O}}$ (M_{EO})	P_{H_2O} (bar)	$X_{0_{CO_2}}$ (10^{-2} wt %)	P_{CO_2} (bar)	Distance From the Sun (AU)	Absorbed Solar Flux $F_{\odot}$ (W m^{-2})	Atmosphere
Figure 2	1.4	0.371	99.7	5	357.3	1	194	grey
Figure 4	2.3	0.621	167	5	357.3	0.77 and 1.30	328 and 115	grey
Figure 5	2.3	0.621	167	5	357.3	0.77 and 1.30	328 and 115	grey
Figure 6	2.3	0.621	167	1 and 10	71.5 and 715	0.77 and 1.00	328 and 194	grey
Figure 7	2.3	0.621	167	0.1–14	7–1000	0.63–1.30	490–115	grey
Figure 8	2.3	0.621	167	0.1–14	7–1000	0.63–1.30	490–115	grey
Figure 9	0.7 and 2.3	0.186 and 0.621	50 and 167	5	357.3	0.77 and 1.00	328 and 194	grey
Figure 10	0.12–4.67	0.031–1.243	8.35–334	0.1–14	7–1000	0.63–1.30	490–115	grey
Figure 11	0.12–4.67	0.031–1.243	8.35–334	0.1–14	7–1000	0.63–1.30	490–115	grey
Figure 12	0.12–4.67	0.031–1.243	8.35–334	0.1–14	7–1000	0.63–1.30	490–115	grey and nongrey
Figure 13	0.12 and 4.67	0.031 and 1.243	8.35 and 334	0.1–14	7–1000	0.63–1.30	490–115	grey
Figure 14	0.12–4.67	0.031–1.243	8.35–334	0.1–14	7–1000	0.63–1.30	490–115	grey
Figure 15	2.3	0.621	167	5	357.3	1	194	grey and nongrey
Figure 16[a]	2.3	0.621	167	0.1	7	1	194	grey
Figure 17	0.12–4.67	0.031–1.243	8.35–334	0.1–14	7–1000	1	194	nongrey
Figure 18	3.76	1	269	1.25	90	0.72	$\mathcal{F}_{t=0} - \mathcal{F}_{t=4.56}$ and $\alpha = 0.2 - 0.7$	nongrey
Figure 19	ppm and 3.76	ppm and 1	ppm and 269	1.25	90	0.72	$\mathcal{F}_{t=0} - \mathcal{F}_{t=4.56}$ and $\alpha = 0.2 - 0.7$	nongrey

[a]All simulations are cloud free excepted in Figure 16.

on Earth (0.03 – 1.24 M_{EO}), corresponding to partial pressures of 8 bar and 333 bar, equivalent to 1.17×10^{-3} and 4.67×10^{-2} weight percent (wt %) of water, respectively. About the initial CO_2 content, we vary the concentration from 10^{-3} to 14×10^{-2} wt % (written $[CO_2]_{t0}$), corresponding to partial pressures varying between approximately 5 and 1000 bar (note that Venus has a surface pressure of 92 bar and more than 95% of CO_2 in the atmosphere).

3. Results

All calculations thereafter simulate an Earth-like planet with the same mass, density, radius, gravity, solidus, and liquidus depth profiles and starting with an entire molten mantle. We consider that these Earth-like planets are orbiting a young Sun. Our calculations follow the grey approximation in most cases.

3.1. Thermal Evolution for Different Solar Distances

Figure 5 shows a standard thermal evolution for a given volatile content and two different solar distances. In the totally liquid magma ocean ($\phi = 1$, $T_{pot} \geq T_{liq}$), heat is evacuated efficiently through vigorous convective motions (see Figures 5a – 5d) which allow efficient volatile degassing (left part of Figures 5e and 5f). As shown in the left part of Figures 5a and 5b, during this early stage, surface and potential temperatures decrease together with time. As cooling proceeds, solidification occurs from the base of the mantle to the surface (section 2.1.1). With crystallization, the liquid fraction decreases, which increases viscosity and slows down convection efficiency inducing a decrease of the convective heat flux coming from the mantle F_{conv} (Figures 5c and 5d). The infrared flux going out of the atmosphere, F_{IR} (or OLR), characterizing the global cooling of the planet (including the atmosphere), is controlled by F_{conv} at early times. When F_{conv} becomes negligible compared to the absorbed solar flux $F_{\odot}$, F_{IR} is then controlled by the solar flux (right part of Figures 5c and 5d). If no significant temporal variation of $F_{\odot}$ (and so of F_{IR}) occurs on the cooling time scale, the planet then evolves in a quasi steady state, all variables remaining more or less constant.

We consider that when the convective heat flux from the mantle becomes an order of magnitude lower than the absorbed solar flux ($F_{conv} \leq 0.1 \times F_{\odot}$), the end of the rapid cooling stage ("ERCS") is reached. This particular time is indicated by a vertical dotted line in our figures. The planet has then evacuated most of its internal heat and both the outgoing longwave radiation F_{IR} and surface temperature T_{surf} are controlled almost solely by the absorbed solar flux $F_{\odot}$.

So a MO will always undergo two different dynamic regimes:

1. Before ERCS, a stage comparable to the "soft magma ocean" of *Abe* [1993] is characterized by efficient MO convection, formation of the atmosphere, strong decrease of surface and potential temperatures, solidification from the bottom to the top of the magma ocean, and decrease of the heat fluxes. Surface conditions are controlled by the cooling of the mantle, and the solar distance is not the main parameter controlling thermal evolution. This first regime ends at ERCS and sets the surface conditions of the planet for its future geodynamic evolution.
2. After ERCS, the surface temperature T_{surf} and the outgoing thermal flux F_{IR} are mainly controlled by the incident solar flux $F_{\odot}$ ($F_{IR} \approx F_{\odot}$) and by the atmospheric volatile content. As the main variables are related to $F_{\odot}$ which evolves slowly with time, this second regime can be consider as a quasi steady state regime (even if the surface is still partially molten in some cases) and the atmospheric composition do not evolve significantly (right part of our figures). The OLR is approximately equal to the absorbed solar flux (global radiative balance).

Thus, depending on $F_{\odot}$ (or solar distance), different surface conditions may exist at ERCS, as illustrated in Figures 4 and 5:

1. At large planet-star distances, the surface of the planet is solid, $T_{surf} < T_{sol}$ (blue curves in Figures 4 and 5, corresponding to a planet located at 1.30 AU). Potential temperature can still be higher than the solidus with remaining melt. Depending on *P-T* surface conditions (or atmospheric volatile content), the moist troposphere can extend to the surface (Figure 4b) and a water ocean can form (type I planets [*Hamano et al.*, 2015; *Lebrun et al.*, 2013]).
2. If the planet is close enough to the star, the surface of the planet is partially molten with $T_{sol} < T_{surf} < T_{liq}$ (red curves in Figures 4 and 5). The planet remains for longer in the magma ocean stage, and convection continues until T_{pot} reaches T_{surf}. The quasi steady state following ERCS implying a molten surface over most

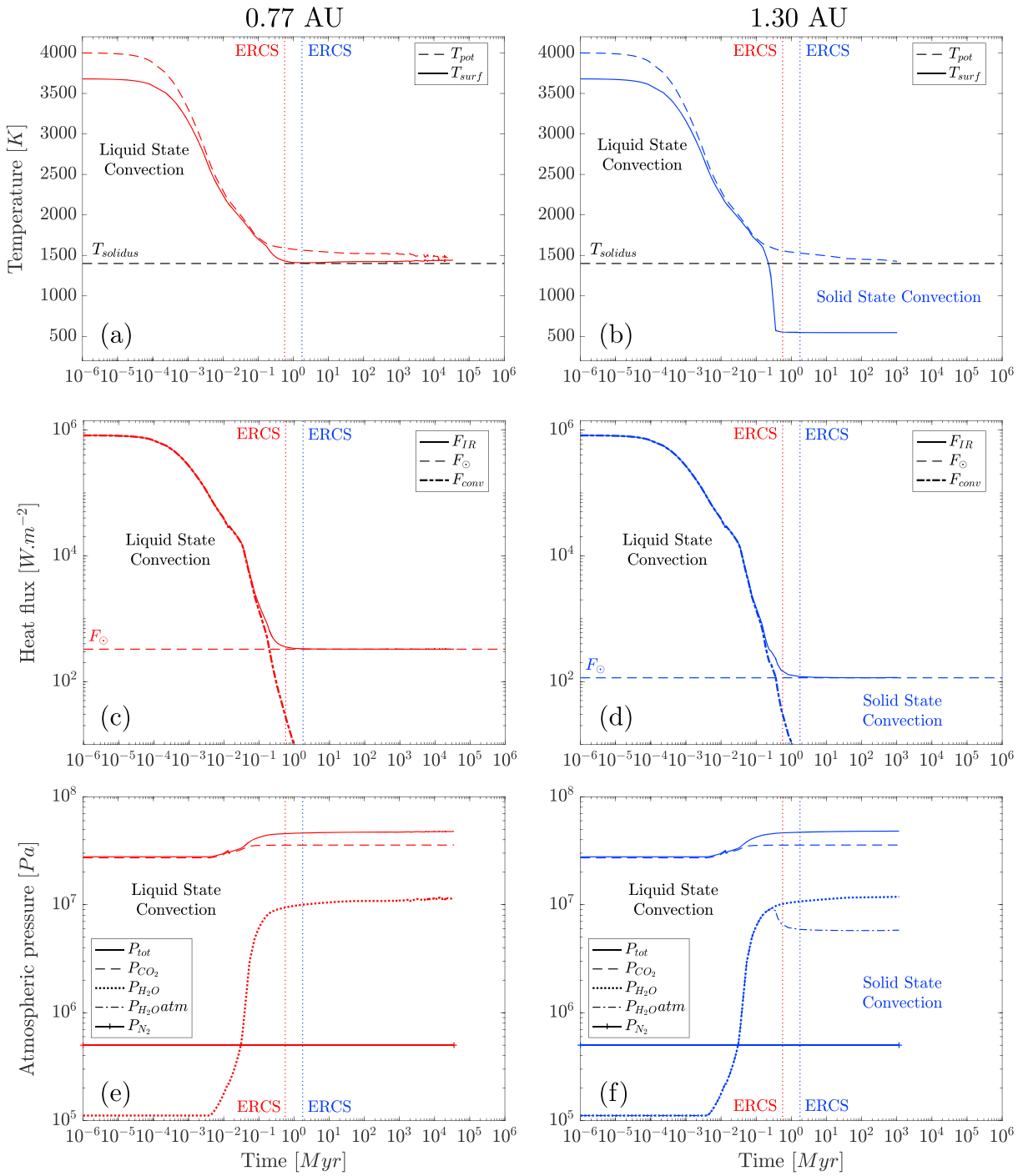


Figure 5. Thermal evolution of the magma ocean for two different distances from the Sun: 0.77 AU (a, c, and e, red) and 1.30 AU (b, d, and f, blue), grey atmosphere, without clouds, $[H_2O]_{t0} = 0.621\ M_{EO}$, $[CO_2]_{t0} = 5 \times 10^{-2}$ wt %. ERCS is indicated by the vertical dotted lines. P_{H_2O}atm corresponds to the uncondensed H_2O partial pressure remaining in the atmosphere if condensation occurs at surface and stores water in the oceans (here a 480 m deep water ocean is formed at 1.30 AU). Corresponding thermal atmospheric profiles at ERCS are shown in Figure 4. Parameters used for the calculations are given in Table 2.

of the lifetime of the planet as long as no volatile escape occurs in the upper atmosphere (type II planets [*Hamano et al.*, 2015; *Lebrun et al.*, 2013]).

3. Another hypothetical case could be considered if the planet is very close to the star: the surface of the planet might be totally liquid ($T_{surf} > T_{liq}$). The planet would stay molten over its entire lifetime even if the convection ends, when all the internal flux will have been evacuated, at $T_{pot} = T_{surf}$ and $Ra < 650$.

ERCS definition allows for comparison between different surface conditions of planets at the same evolution stage. Introducing this newly defined particular time is more appropriate than using the end of the magma ocean phase which is not always reached, particularly for planets close to their star.

3.2. Influence of the Initial CO_2 Content

We conducted calculations for a large range of H_2O and CO_2 contents. We first investigate the effect of the CO_2 content for a given water content fixed at 0.6 Earth ocean. At early times, whatever the solar distance, the surface temperature T_{surf} and the outgoing infrared flux F_{IR} are respectively higher and lower for high CO_2 contents (red curves in Figure 6) than for low CO_2 concentrations (blue curves in Figure 6). Due to a lower solubility of CO_2 in the melt than H_2O (Appendix C), most of CO_2 is degassed earlier than H_2O (Figures 6e and 6f). Thus, at early times, CO_2 is the major component of the atmosphere and controls its opacity. Acting alone as a greenhouse gas, carbon dioxide tends to increase the surface temperature. This blanketing effect explains why the surface temperature is higher at early times for $[CO_2]_{t0}=10^{-1}$ wt % (Figures 6a and 6b). As degassing proceeds, P_{H_2O} increases while P_{CO_2} remains almost constant in the atmosphere (Figures 6e and 6f), thus increasing the humidity ratio H_2O/CO_2, as well as the mixing ratio ($P_{H_2O}/(P_{CO_2} + P_{N_2})$), and atmosphere's opacity.

At 0.77 AU, because water does not condense, the humidity ratio at ERCS is higher, in turn inducing a higher opacity for lower initial CO_2 content (Figures 6a and 6c). The mesosphere is thinner in that case, its bottom altitude is higher (Figure 6g) and following the tropospheres' adiabatic gradients, it results in a higher surface temperature at ERCS (Figure 6a).

At 1 AU, the moist troposphere extends to the surface in Figure 6h: saturation vapor pressure is reached at the surface for $[CO_2]_{t0} = 10^{-2}$ wt %. The formation of an ocean then causes an important decrease of atmospheric P_{H_2O}atm, while all H_2O remains in vapor phase for the higher $[CO_2]_{t0}$, when no ocean is formed (Figure 6f). Thus, at 1 AU and for the same initial water content, because of water ocean's formation, the humidity ratio is lower for low CO_2 than for high CO_2 content. It decreases the atmosphere's opacity and results in a lower mesosphere's bottom altitude (Figure 6h) and a colder surface temperature in that case (Figure 6b). Also, note that ERCS is reached less abruptly for higher initial CO_2 contents. Indeed, when condensation occurs, increasing the CO_2 content counteracts the effect of rapid H_2O vapor trap through condensation process.

Figure 7 summarizes surface conditions at ERCS for various initial CO_2 contents and for solar distances ranging from 0.63 to 1.30 AU. Above a certain $[CO_2]_{t0}$ threshold (5×10^{-2} wt % corresponding to P_{CO_2}=357 bar), water condensation strongly depends on CO_2 content, whereas below this value, it only depends on the solar distance. A third type of planetary surface might exist at ERCS: far from the Sun, and for high CO_2 contents, this type III planet has a solid surface and no water ocean (orange area of Figure 7), thus differing from the type I planets of *Hamano et al.* [2013].

Concerning surface temperatures, two opposite behaviors arise from either side of the critical distance D_C: far from the star ($D > D_C$), increasing CO_2 induces higher surface temperatures, close to the star ($D < D_C$), increasing the CO_2 content lowers surface temperatures at ERCS (Figure 7). Indeed, as explained before, the opacity τ of the radiative layers in the upper atmosphere, and thus the blanketing effect, depend on the humidity ratio H_2O/CO_2. As H_2O absorption is higher, an increase in CO_2 "dilutes" the water vapor thus decreasing the atmosphere's opacity. Atmosphere is then more transparent to thermal radiation for higher CO_2 content, which induces lower surface temperatures as heat is more efficiently evacuated to space. Conversely, beyond D_C where water can condense, increasing CO_2 prevents water condensation and favors an increase of atmospheric water vapor, thus increasing the blanketing effect and warming the surface.

In fact, the surface temperature depends on the atmospheric vertical structure. Figure 8 shows the altitude of the tropopause (i.e., the base of the mesosphere), which is related to the thermal transparency of the atmosphere, and indicates from where thermal radiation is emitted. If the blanketing effect of the atmosphere is important, the altitude where the optical depth, $\langle\tau\rangle_\lambda$, is equal to 2/3 is high, as well as the surface temperature.

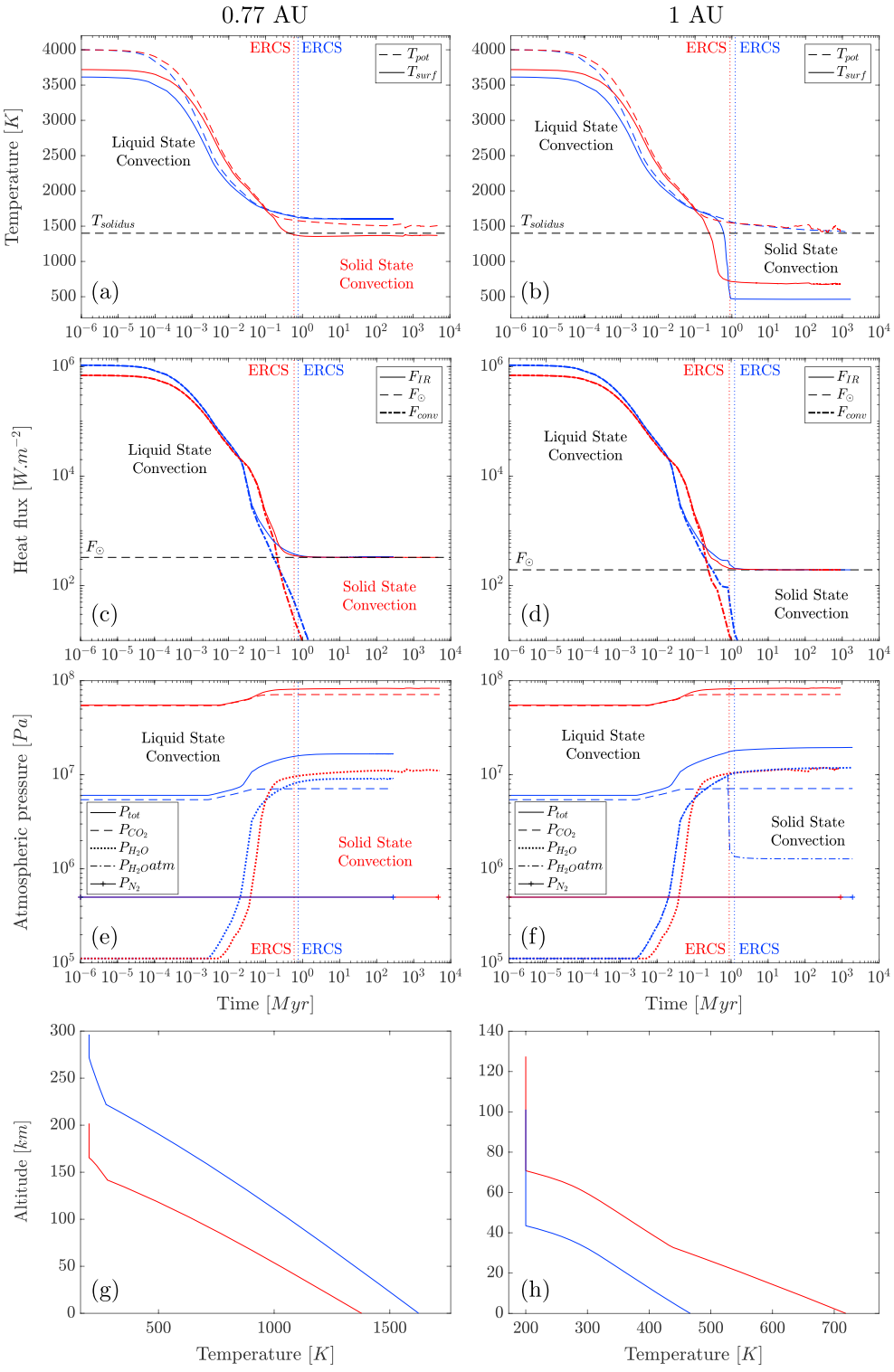


Figure 6. Thermal evolution of the magma ocean for two different initial CO_2 contents: 10^{-2} (blue curves) and 10^{-1} wt % (red curves), and two different solar distances: 0.77 AU (a, c, e, and g, crosses in Figures 7 and 8) and 1 AU (b, d, f, and h, squares in Figures 7 and 8), grey radiative-convective atmosphere, without clouds, $[H_2O]_{t0} = 0.621\ M_{EO}$. At ERCS, for $D = 0.77$ AU, $P_{H_2O}/P_{CO_2} = 1.17$ for $[CO_2]_{t0} = 10^{-2}$ wt % and $P_{H_2O}/P_{CO_2} = 0.13$ for $[CO_2]_{t0} = 10^{-1}$ wt %. For D=1 AU, $P_{H_2O}/P_{CO_2} = 0.19$ for $[CO_2]_{t0} = 10^{-2}$ wt % and $P_{H_2O}/P_{CO_2} = 0.145$ for $[CO_2]_{t0} = 10^{-1}$ wt %. At 1 AU, for $[H_2O]_{t0} = 0.621\ M_{EO}$ and $[CO_2]_{t0} = 10^{-2}$ wt %, a 910 m deep water ocean is formed at ERCS. Parameters used for the calculations are given in Table 2.

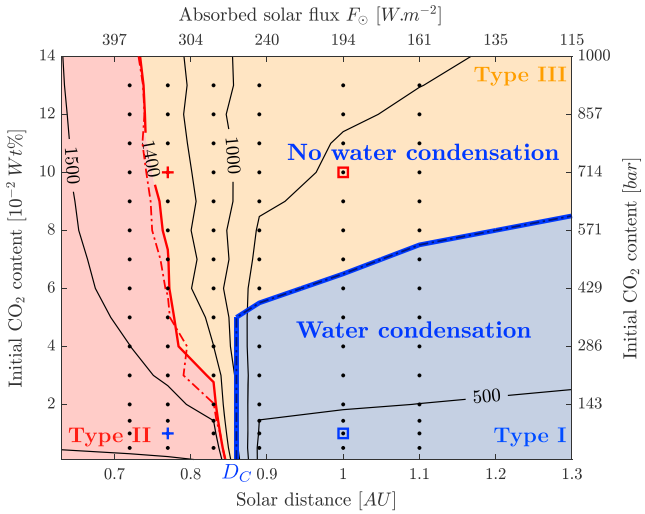


Figure 7. Surface temperature isotherms (black lines) and solidus temperature (red line) as a function of CO_2 content and solar distance at ERCS. Below water condensation limit (blue line), a water ocean can condense at the surface of the planet. Crosses and squares correspond to calculations shown on Figure 6. The different types of planet are represented by colored areas. The dashed lines stand for the limits obtained by considering a secular cooling only occurring over the liquid-state mantle (i.e., between the solidification front R_S and the surface, see section 2.1.3 and Appendix B). Parameters used for the calculations are given in Table 2.

Conversely, when the atmosphere is more transparent, i.e., for a lower humidity ratio, this altitude decreases. From this altitude downward, the lapse rates within the underlying layers sets surface temperature (e.g., Figure 6g). If a water ocean is formed, i.e., the moist troposphere reaches the surface, atmospheric opacity is lower, as well as surface temperatures. It thus explains well the strong correlation between surface temperatures and altitude of the tropopause.

3.3. Influence of the Initial H_2O Content

We conduct the same sensibility study for various initial water contents. Figure 9 compares the time evolution of the main variables for two representative solar distances and two representative water contents with a fixed CO_2 concentration. As discussed in section 3.2, the atmospheric thermal structure depends on the

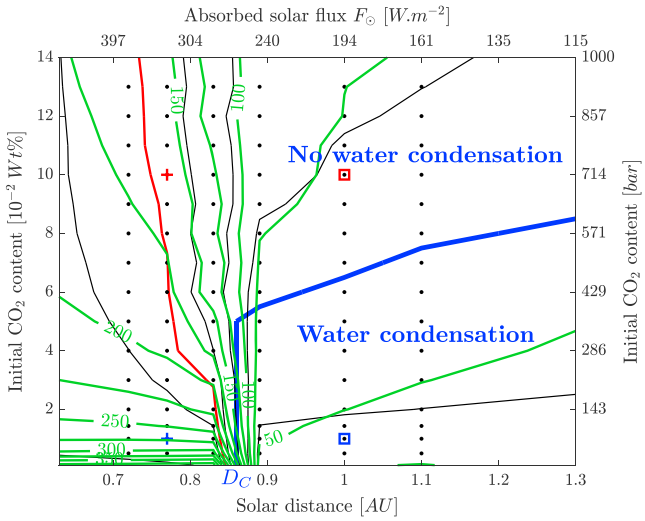


Figure 8. Water condensation limit (blue line), surface temperature isotherms (black lines), and solidus temperature (red line) compared to the altitude of the tropopause (green isolines) as a function of the CO_2 content and solar distance at ERCS. The green lines also correspond to the altitude where the optical depth $\langle\tau\rangle_\lambda = 2/3$: mesosphere's bottom altitude, which can be understood as a direct measure of the atmospheric opacity. Grey atmosphere, cloud free. Parameters used for the calculations are given in Table 2.

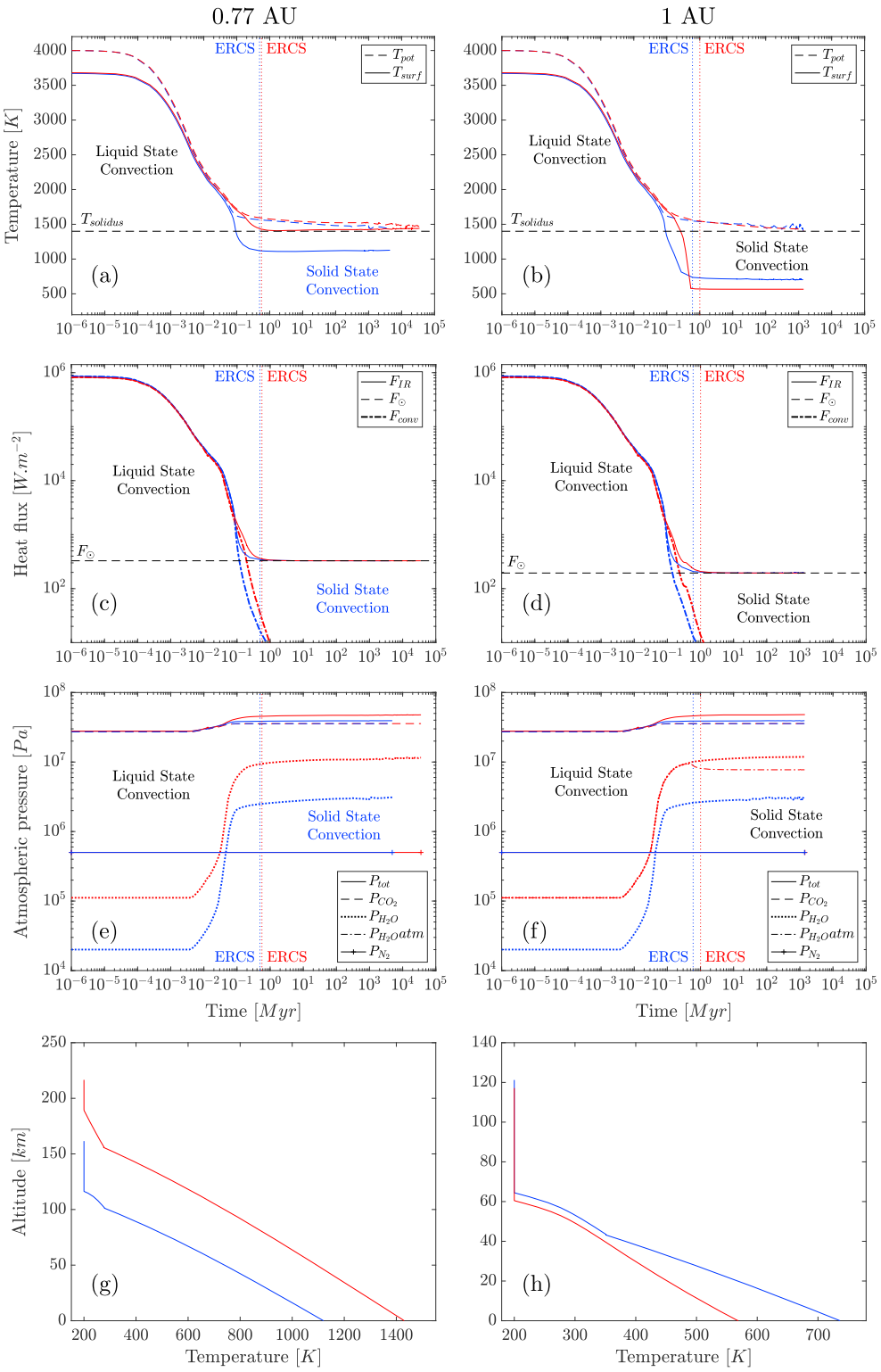


Figure 9. Thermal evolution of the magma ocean for two water contents: 0.186 (blue curves) and 0.621 M_{EO} (red curves), for a grey radiative-convective atmosphere, at 0.77 AU (a, c, e, and g, crosses in Figure 10) and 1 AU from the Sun (b, d, f, and h, squares in Figure 10), $[CO_2]_{t0} = 5 \times 10^{-2}$ wt %. At ERCS, for $D = 0.77$ AU, $P_{H_2O}/P_{CO_2} = 0.07$ for $[H_2O]_{t0} = 0.186$ M_{EO} and $P_{H_2O}/P_{CO_2} = 0.265$ for $[H_2O]_{t0} = 0.621$ M_{EO}. For $D = 1$ AU, $P_{H_2O}/P_{CO_2} = 0.073$ for $[H_2O]_{t0} = 0.186$ M_{EO} and $P_{H_2O}/P_{CO_2} = 0.226$ for $[H_2O]_{t0} = 0.621$ M_{EO}. At 1 AU and for $[H_2O]_{t0} = 0.621$ M_{EO}, a 243 m deep water ocean is formed at ERCS. Parameters used for the calculations are given in Table 2.

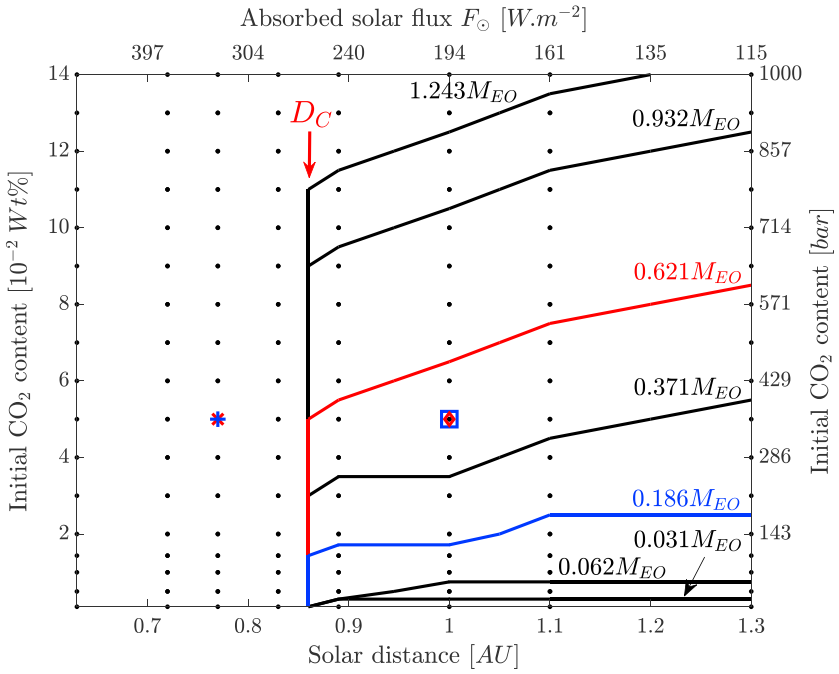


Figure 10. Regime diagram indicating the state of the water at ERCS on an Earth-like planet for different water contents. Above the condensation limits (lines), no water condensation occurs at the surface, while below those limits, a water ocean is present at ERCS time. The crosses and the squares are analyzed in Figure 9 using the same color code. Parameters used in the calculations are given in Table 2.

vertical layering and specifically on the altitude of the tropopause. Below the radiative mesosphere, the temperature profile follows the moist and dry adiabatic lapse rates. Regarding opacity, increasing H_2O is similar to decreasing CO_2 (as humidity ratio is defined as H_2O/CO_2); thus, we obtain opposite behaviors for the two components.

At early times, whatever the distance, higher H_2O content increases atmosphere's opacity, thus decreases F_{IR} (Figures 9c and 9d), and as moist troposphere is thin at that moment, it results in higher surface temperature (as previously described for CO_2).

Close to the star (Figures 9a, 9c, 9e, and 9g), where no condensation occurs and as degassing proceeds, humidity ratio, and so opacity, is always greater for $[H_2O]_{t0} = 0.621\ M_{EO}$ than for $[H_2O]_{t0} = 0.186\ M_{EO}$. More water vapor in the atmosphere results in a higher tropopause and surface temperature (Figure 9g). Conversely, at 1 AU (Figures 9b, 9d, 9f, and 9h), where condensation occurs for $[H_2O]_{t0} = 0.621\ M_{EO}$, atmospheric P_{H_2O}atm strongly decreases (Figure 9f), opacity becomes lower than for $[H_2O]_{t0} = 0.186\ M_{EO}$: the resulting surface temperature is lower for higher water content.

It is important to note that beyond D_C, even if no ocean is formed at the surface (above the condensation limit), higher water contents lead to thicker moist troposphere. The adiabatic lapse rate being steeper in the dry troposphere than in the moist troposphere, it may result in lower surface temperatures for higher water contents (Figure 13).

Condensation limits at ERCS as a function of solar distance and CO_2 content are plotted in Figure 10 for various initial H_2O contents. Water condensation depends both on CO_2 and H_2O as the limits are different for distinct water contents. Note that the critical distance $D_C = 0.86 \pm 0.3$ AU (red arrow in Figure 10, similar to the one calculated by *Hamano et al.* [2015]) remains constant whatever the volatile content and so does the associated equilibrium temperature. What changes is the CO_2 concentration threshold above which water does not condense at D_C, distance beyond which water condensation strongly depends on the volatile content. Increasing water content extends the CO_2 concentration range for which condensation is possible, the pressure effect controlling water condensation at the surface (with higher P_{H_2O}, saturation vapor pressure at the surface can be reached for higher CO_2 concentrations).

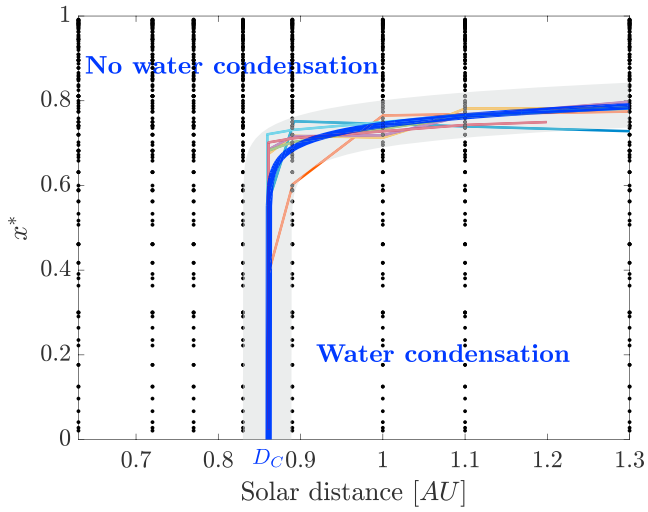


Figure 11. Regime diagram indicating the state of the water at ERCS on an Earth-like planet using our dimensionless parameter x^* for the volatiles (equation (11)). The different lines correspond to the condensation limits obtained for different water contents (Figure 10). The blue line is the fit representing those data with the associated uncertainties in the grey area.

3.4. Scaling Laws

As all condensation limits have similar shapes (Figure 10), it shows that condensation might depend on a single parameter involving a combination of volatile content. It is natural to introduce a dimensionless parameter such as

$$x^* = \frac{P_{CO_2}}{P_{CO_2} + P_{H_2O}}, \tag{11}$$

with x^* representing the initial relative volatile content expressed in terms of equivalent atmospheric pressures P_{CO_2} and P_{H_2O}. Figure 11 shows that all the curves of Figure 10 now collapse on the same master curve when using this new scale for the CO_2 content.

As previously discussed, the condensation limit is a function of the absorbed solar flux and of the greenhouse gases budget in the atmosphere. Conversely, the location of the critical distance D_C (i.e., the "classical" inner edge of the habitable zone, Figure 10) only depends on the amount of energy received at the surface of the planet. For a given planetary system, it results in the combination of the solar constant $\mathcal{F}_0$, specific to the host star, and the bolometric albedo α, depending on the characteristics of the surface and atmosphere and also on the spectral energy distribution of the star. In order to extrapolate our predictions to other stellar systems, we conducted another set of calculations for different stellar and planetary conditions: planets with albedo ranging from 0.1 to 0.7, stellar constant varying from the young Sun to the present-day value. For this range of parameters, whatever the combination of α and $\mathcal{F}_0$, the equilibrium temperature associated to D_C is constant and equal to 261 $\pm$ 5 K. These calculations are shown in Figure 12a. This value is similar to the value corresponding to the inner edge of habitable zone found in other studies with different models and approaches [*Kopparapu et al.*, 2013; *Selsis et al.*, 2007]. The corresponding outgoing infrared flux $F_C = \sigma T_{eqC}^4$ is close to the Nakajima's limit value (radiation limit of steam atmospheres [*Hamano et al.*, 2015]). This critical equilibrium temperature T_{eqC} can be used to define the critical distance D_C at ERCS for a given planetary system:

$$D_C = \sqrt{\frac{\mathcal{F}_0(1-\alpha)}{\sigma T_{eqC}^4}}. \tag{12}$$

The dimensionless stellar distance D^* of a planet of a given albedo is then

$$D^* = \frac{D}{D_C}. \tag{13}$$

If D^* is greater than one, the planet is located farther than the critical distance and condensation may occur at the surface of the planet at least for low enough values of x^* (i.e., sufficiently wet planets).

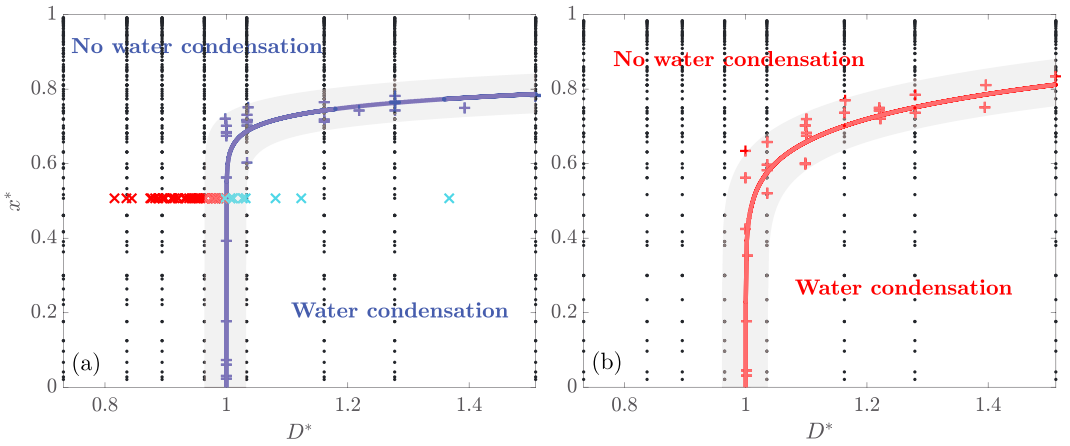


Figure 12. Condensation limits for different H_2O contents as a function of the dimensionless star-planet distance (D^*, equation (13)) for a (a) grey radiative-convective and (b) nongrey *k*-correlated atmosphere. The plus signs correspond to the condensation limits obtained for different water contents and the cross markers stand for calculations made for different albedos and solar constants ranging respectively from 0.1 to 0.7 and from the young Sun's solar constant to the present-day value. Cross markers are blue if water condensation occurs and red if not. Parameters used for the calculations are given in Table 2.

Fitting all the data leads to an expression for the water condensation limit:

$$x_C^* = a \times (D^* - 1)^n, \tag{14}$$

with $a = 0.82 \pm 0.03$, $n = 0.05 \pm 0.035$ for the grey approximation. We also apply our approach to the nongrey *k*-correlated atmospheric model. In this case, $a = 0.902 \pm 0.4$, $n = 0.128 \pm 0.02$. The shape of these limits are similar in both cases (for discussion about the differences between these two atmospheric treatments, see section 4.1).

Using variables D^* and x^*, it is possible to predict water condensation for different stellar radiations and different atmospheric compositions of different planets. Conversely, knowing if liquid water exists or not at a planetary surface allows to infer a plausible corresponding range of initial volatile content.

Obviously, limitations exist about these predictions: for example, beyond a certain amount of volatiles in the atmosphere, the state of the matter, and more specifically the gas properties at very high pressures (supercritical fluids) remain poorly understood. However, the radiative layers are located in the uppermost atmosphere, where low-pressure conditions are well known. The main limitation of our simple model comes from the lack of feedbacks between atmospheric composition and albedo (see section 4.3).

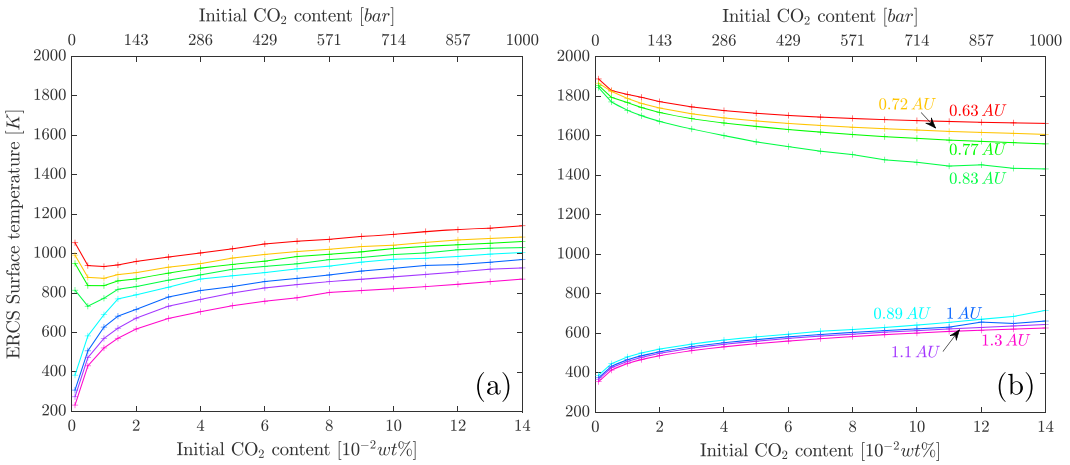


Figure 13. Surface temperatures obtained at ERCS for solar distances varying from 0.63 to 1.30 AU, initial CO_2 contents from 0.1 to 14×10^{-2} wt % and initial water contents equal to (a) 0.031 M_{EO} and (b) 1.243 M_{EO}. Parameters used for the calculations are given in Table 2.

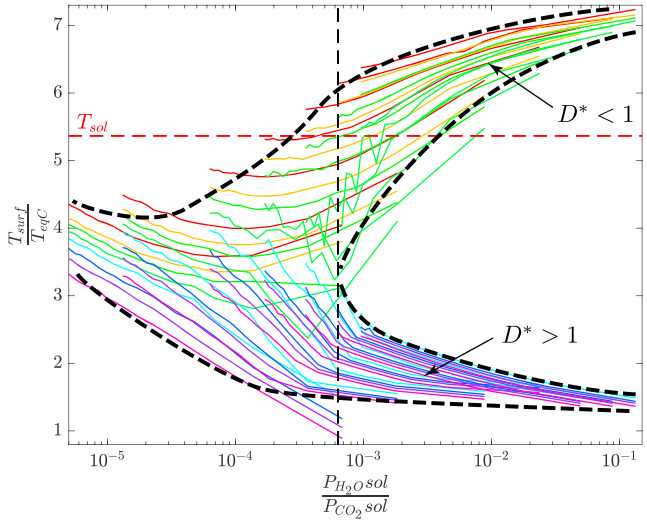


Figure 14. Surface temperatures obtained at ERCS for 7 different $[H_2O]_{t0}$, 17 different $[CO_2]_{t0}$, and 8 different solar distances, using our dimensionless variables. The vertical dashed line separates water-dominated (right side) to CO_2-dominated (left side) atmospheres. The red dashed line corresponds to the solidus temperature; it separates planets with a molten surface (upper part) to planets with a solid surface at ERCS. Parameters used for the calculations are given in Table 2.

Despite these uncertainties, one can look at ERCS temperatures as a function of volatile content for different distances to the Sun (Figure 13). As previously shown in Figure 7, two distinct trends arise from either side of the critical distance separating type I and type II hot planets. As discussed in the previous sections, atmospheric composition controls surface temperatures through two parameters: the opacity of the radiative layer and the adiabatic lapse rates in the underlying convective layers. As opacity is a function of the humidity ratio H_2O/CO_2, it might be used to scale the volatile content. Rather than using the initial contents or the equivalent atmospheric pressures, we used the partial pressures given by the solubility laws (see Appendix C) that are more representative of degassing and so of the atmospheric composition (note that using calculated partial pressures at ERCS would not be predictive). We then normalized surface temperatures by the critical equilibrium temperature of the system T_{eqC}. For H_2O-dominated atmospheres (right side of the vertical dashed line in Figure 14), corresponding to $x^* < 0.8$, two distinct trends arise from either side of the critical distance separating type I and type II hot planets. Nearest planets from the Sun with water enriched atmosphere reach ERCS with a molten surface ($T_{surf} > T_{sol}$, upper part of Figure 14). For CO_2-dominated atmospheres (left part of Figure 14), no water ocean is formed at ERCS and a strong greenhouse effect results in high surface temperatures but is not sufficient to sustain a molten surface (type III planets). For those atmospheres, the atmospheric composition determines water condensation instead of the distance for H_2O-dominated atmospheres. Note that the green oscillating curve corresponds to a planet located at 0.83 AU, close to the critical distance, possibly being a source of numerical instabilities.

4. Discussion

4.1. Grey Radiative-Convective Versus Nongrey (*k*-Correlated) Atmosphere

In our atmospheric model, longwave radiation (from wave number $\sigma = 0$ cm^{-1} to $\sigma = 10,100$ cm^{-1}) can be computed either using the grey approximation or using a *k*-correlated radiative transfer code. The grey approximation uses constant mass absorption coefficients for H_2O and CO_2 over all this spectral range: $k_{H_2O} = 10^{-2}$ m^2 kg^{-1} and $k_{CO_2} = 10^{-4}$ m^2 kg^{-1} following *Nakajima et al.* [1992]. H_2O absorption is greater than CO_2 due to more absorption bands in the thermal spectrum. In contrast, mass absorption coefficients used in the *k*-correlated model depend on wavelength, H_2O/CO_2 ratio, temperature, and total pressure for H_2O and CO_2 and are based on high-resolution spectrum computed by KSPECTRUM [*Eymet et al.*, 2016; see *Marcq*, 2012; *Marcq et al.*, 2017]. These higher-resolution spectra lead to lower absorption for H_2O. However, using the grey radiative-convective model allows exploratory simulations that are helpful to precise conditions to implement in the *k*-correlated model.

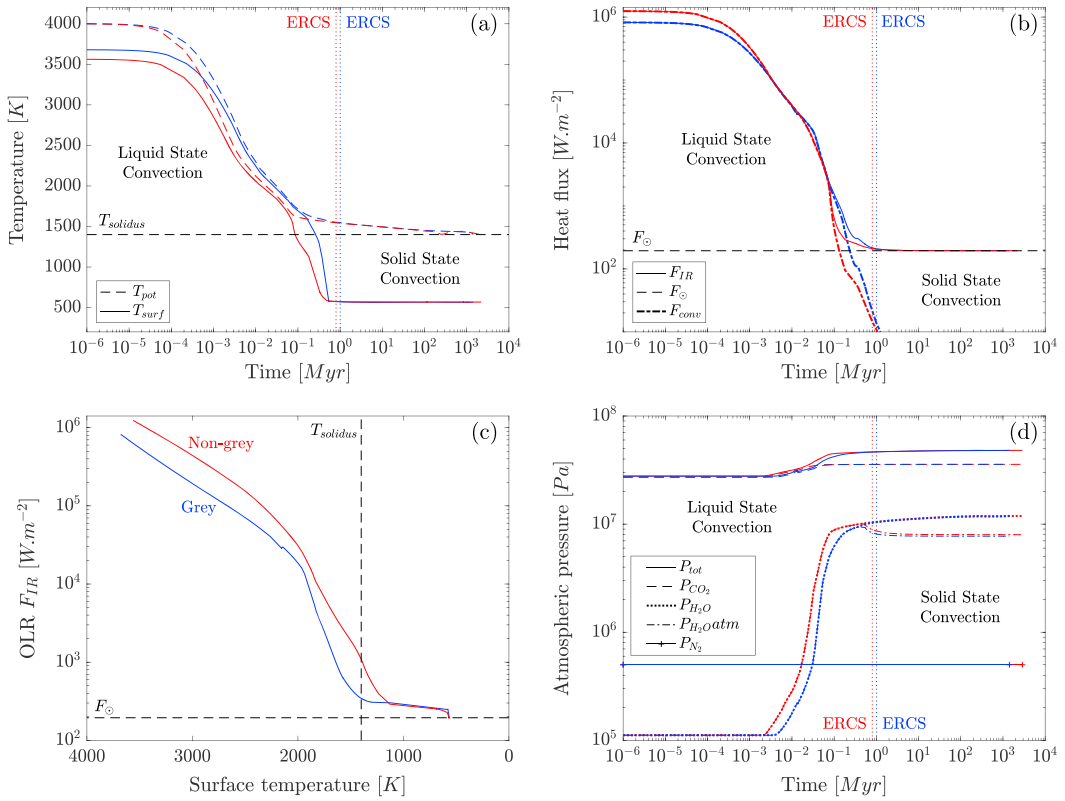


Figure 15. Thermal evolution of the magma ocean when the atmosphere is treated as a radiative-convective grey atmosphere (blue lines, 234 m deep ocean at ERCS) and with our radiative-convective *k*-correlated model (red lines, 159 m deep ocean at ERCS). $D = 1$ AU, $[H_2O]_{t0} = 0.621$ M_{EO}, $[CO_2]_{t0} = 5 \times 10^{-2}$ wt %, cloud free. Parameters used for the calculations are given in Table 2.

At early times, a grey atmosphere underestimates the outgoing longwave radiation (F_{IR}) compared to a non-grey atmosphere (Figure 15b). It results in a higher surface temperature. This surface temperature difference remains until water ocean formation at ERCS. Just after ERCS, humidity ratio decreases as well as atmospheric opacity. Condensation at the surface stores an important amount of water in the ocean, and condensed water contributes far less to the radiative transfer within the atmosphere. Heat transfer throughout the atmosphere is controlled by the convective adiabatic lapse rate which does not depend on absorption coefficients. Hence, the temperatures are similar in the grey or nongrey case.

To summarize, closer to the star than D_C, atmospheric opacity is important (Figure 8) and surface temperatures depend on the mass absorption coefficients used. Conversely, when water ocean condensation is possible, i.e., beyond D_C, humidity ratio strongly decreases as well as atmosphere's opacity (Figure 8) which is then controlled by the low CO_2 absorption coefficients (both in the grey and nongrey approximation).

If water condensation occurs ($D > D_C$), surface temperatures predictions are similar when using either fixed mass absorption coefficients or *k*-correlated coefficients. But for $D < D_C$, using H_2O *k*-correlated coefficients allows better surface temperatures estimates, the grey approximation might overestimate surface temperatures and may slightly shift the water condensation's limit to larger solar distances and lower CO_2 contents as shown in Figure 12 (for example, at $D^* = 1$, a CO_2 content corresponding to $x^* = 0.6$ is enough to condense water, but not in the nongrey case).

4.2. Influence of the Clouds

The effect of clouds (present in the moist troposphere) on shortwave radiation are parameterized through a bolometric albedo [see *Marcq et al.*, 2017] and computed with the four-steam DISORT radiative transfer code for longwave radiation [*Stamnes et al.*, 1988]. The user can choose to take into account, or not, the effect of clouds on thermal radiation.

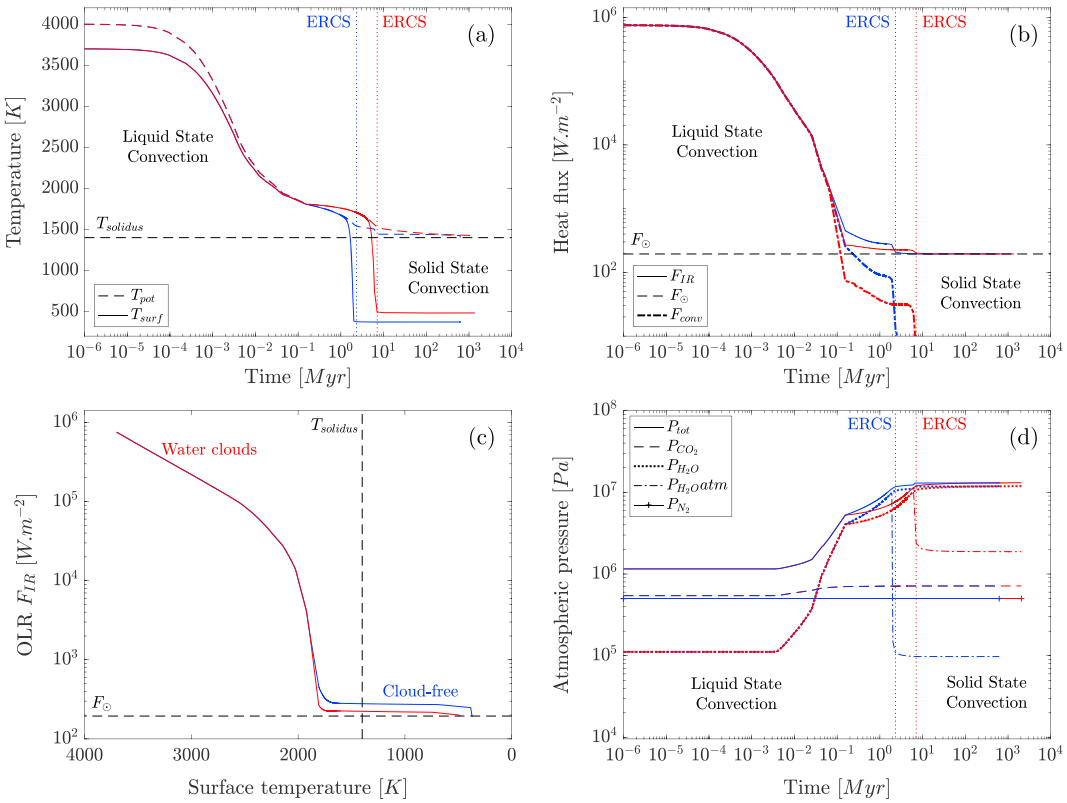


Figure 16. Comparison of the thermal evolution of a magma ocean with a grey radiative-convective atmosphere, without (blue) and with water clouds (red). D = 1 AU, $[H_2O]_{t0}$ = 0.621 M_{EO}, $[CO_2]_{t0} = 10^{-3}$ wt %. With water clouds, a 836 m deep ocean is formed, without clouds a 1042 m deep ocean is formed at ERCS. Parameters used for the calculations are given in Table 2.

Strong uncertainties are associated with this parameter in Earth's energy budget computations and in atmospheric studies in general (heating or cooling effect of the global cloud cover). Furthermore, to constrain the cloud effect on a global scale, 3-D climate models are required, taking into account both clouds global dynamic and spatial distribution. With our 1-D model, we are neither able to include partial cloud coverage or to parameterize microphysical cloud properties (see *Marcq et al.* [2017] and *Kopparapu et al.* [2013] for a discussion about the 1-D simulations limits concerning the clouds). Our model can only provide two limits concerning two extreme cases: an atmosphere without clouds or with a 100% cloud coverage (see Figure 16 for a comparison between these two cases).

At early times, surface temperatures are high and moist troposphere, containing clouds, is not thick enough to significantly affect radiative transfer: there is no difference between the two simulations. As the moist troposphere is getting thicker, the thermal effect of the cloud cover increases surface temperature through greenhouse effect, increasing atmospheric opacity, thus decreasing the outgoing infrared flux F_{IR}. The stronger blanketing effect delays ERCS time and the resulting higher surface temperatures (around 100 K in that case) might prevent water condensation at the surface. Nevertheless, we do not take into account the reflectivity of the clouds that should decrease the absorbed solar flux and might balance their blanketing effect. Note that for H_2O-dominated atmospheres presented here, F_{IR} exhibits a strong asymptotic limit as a function of T_{surf} (Figure 16c). As discussed in *Marcq et al.* [2017], such a cloud cover decreases the value of this Nakajima's limit.

4.3. Limitations

Different limitations arise from the assumptions we made to build this coupled model. Concerning the atmosphere, while we have shown that the differences between the grey case and nongrey case are small, using constants absorption coefficients for H_2O and CO_2 may overestimate the opacity and then the surface temperature. We have not considered the blanketing effect of dust particles injected in the atmosphere subsequent

to giant impacts. It should affect the opacity and the resulting surface temperature likewise [*Matsui and Abe*, 1984; *Abe and Matsui*, 1985]. However, for dense atmosphere, and especially H_2O-rich atmosphere, this effect should be negligible due to the already high opacity of these atmospheres.

We do not take into account the effect of shortwave radiation on the radiative budget which is parameterized only through a prescribed value of albedo [*Marcq et al.*, 2017]. It does not allow us to model properly absorption and scattering for other stellar spectral classes. Ongoing improvements are made to better compute feedbacks between atmospheric composition and incident stellar flux. We can mention for example the extension of our spectral range computations to shorter wavelengths in order to test our predictions for stars of different spectral classes, as well as a true computation of the bolometric albedo of the planet taking into account Rayleigh scattering for high CO_2 contents among other things [*Kopparapu et al.*, 2013].

The solar flux received at the surface of a planet is not uniform: the equator—closer to the Sun if the obliquity is small—is more heated than the poles, as well as the dayside compared to the nightside (depending on the rotation rate). We cannot model properly these differences in 1-D and a reasonable approximation is to take an average value of the solar constant for the entire surface of the planet. However, this effect does not affect significantly our results because the Sun is not the main energy source before reaching ERCS, the convective flux from the mantle being then the major heating source of the atmosphere. Nevertheless, for different rotation rates, when the surface temperature is mainly controlled by the incident solar flux (post-ERCS evolution), it can strongly influence surface temperatures and the position of the inner edge of the HZ [*Yang et al.*, 2014; *Kopparapu et al.*, 2016].

Regarding the volatile content, no escape processes are modeled here but the accretion time and the time to reach ERCS are shorter than the characteristic time to lose a consequent amount of H_2O in the outer space [*Abe and Matsui*, 1985]. Furthermore, this process, which desiccates the atmosphere, mostly affects planets located below the critical distance where water condensation do not occur [*Hamano et al.*, 2013], making them more uninhabitable than they already are at ERCS. Conversely, if a water ocean is formed at ERCS, escape processes may not affect significantly atmospheric composition (water being stored in the ocean is not affected by escape processes). Concerning CO_2 atmospheric content, the dissolution of carbon dioxide in the water ocean, once condensed, traps an important amount of CO_2 out of the atmosphere. Carbon dioxide then precipitates and might be reinjected in the mantle, as well as water, through subduction processes, before being degassed again by volcanism. *Foley and Driscoll*'s [2016] review shows the importance to couple all the reservoirs in order to study rocky planets evolution. Also, extending our solar distance range to higher values is limited by the fact that we do not compute neither CO_2 condensation in the atmosphere at low temperatures (see *Kasting* [1991] for consequences of this phenomenon) nor water freezing, even within the clouds.

Considering the internal model, its 1-D nature required simplifications, such as the effect of segregation, rotation and existence of a distinct basal magma ocean, as discussed in section 2.1 and Appendix B. Moreover, other heat sources are neglected here, such as the tidal heating by the new Moon [*Zahnle et al.*, 2007] or reinjection of energy by impacts. Impacts might also affect volatile content by eroding the atmosphere [e.g., *Walker*, 1986; *Ahrens*, 1993] as well as supply volatiles [e.g., *Watkins*, 1983; *O'Brien et al.*, 2014]. Further, 2-D or 3-D models are necessary to characterize those processes and derive the necessary scalings to include in a 1-D model.

5. The Earth and Venus

We now apply our first-order scaling laws to the cases of early Earth and Venus. Even if the sources and processes involved differ to explain water supply during terrestrial planets history [*Marty*, 2012; *Morbidelli et al.*, 2012], one can make the reasonable assumption that the initial water content of Venus and the Earth were not so different at early times [*Raymond et al.*, 2007] and that at least one Earth ocean mass ($[H_2O]_{t0}=1\ M_{EO}$ ($[H_2O]_{t0} \approx 270$ bar) and a Venus present-day CO_2 concentration ($[CO_2]_{t0} \approx 90$ bar) is a reasonable guess for the initial volatile content ($[CO_2]_{t0} \approx 60$ bar for the early Earth following *Holland* [1978]). We also assume an initial MO planet without atmosphere [e.g., *Cameron*, 1983; *Ahrens*, 1993] and a planetary albedo of 0.2. From this initial state (stars in Figures 17 and 19a), we discuss how our first-order model can help to elucidate the evolutionary path of these planets (Figure 19b).

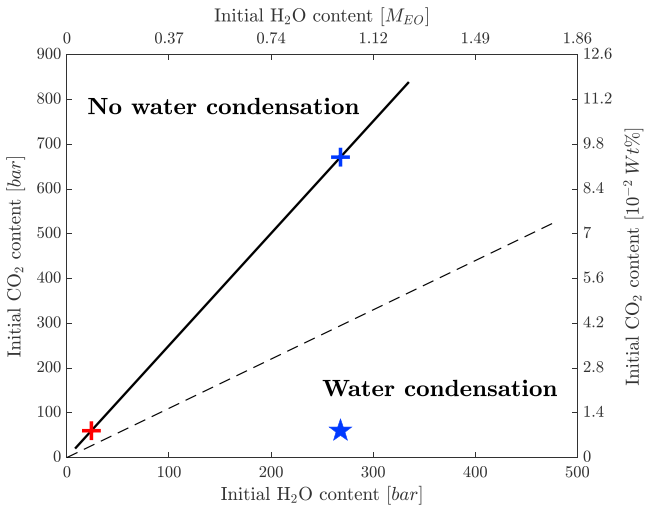


Figure 17. Water condensation diagram for the early Earth ($\alpha = 0.2$, $D = 1$ AU, young Sun) as a function of H_2O and CO_2. Above the condensation limit (black line), CO_2 precludes the formation of a water ocean. The dashed line stands for a chondritic CO_2/H_2O ratio, the blue star represents the early Earth's position, and the crosses the critical volatile contents associated. Parameters used for the calculations are given in Table 2.

5.1. Early Earth

Our results show that the current Earth is indeed located in the HZ (i.e., $D^* > 1$, Figure 19) and that water condensation likely occurred for the early Earth orbiting a faint young Sun (Figures 17 and 19a), which supports the validity of the model. Recent accretionary models combined with geochemical evidences show that water was likely brought to Earth in a proportion that depends on the details of the accretion models [*Raymond et al.*, 2007; *O'Brien et al.*, 2006; *Morbidelli et al.*, 2000] (see also *Morbidelli et al.* [2012] for a review). Figure 17 shows, for an Earth-sized planet orbiting around a solar-type star at a Sun-Earth distance, the quantity of CO_2 required to prevent condensation. As an example, if H_2O and CO_2 are initially in chondritic proportions, formation of an ocean certainly occurred (Figure 17). For 1 M_{EO}, 670 bar of CO_2 is required in order to prevent the formation of a water ocean (blue cross in Figure 17). Conversely, for $[CO_2]_{t0} = 60$ bar, corresponding to the CO_2 presently stored in terrestrial carbonates [e.g., *Holland*, 1978], at least $[H_2O]_{t0} = 0.09\ M_{EO}$ (24 bar) is required to condense water at the surface of the early Earth (red cross in Figure 17).

5.2. Venus

Our study reproduces well the surface conditions existing now on Venus. Despite the fact that Venus is located inside the habitable zone, its high CO_2/H_2O ratio prevents condensation at the surface ($D^* > 1$, Figure 19). As suggested by *Abe and Matsui* [1988], the tiny amount of water in its atmosphere [e.g., *de Bergh et al.*, 1995; 2006] is not sufficient to allow present-day water condensation ($x^* \approx 1$). However, evidences suggest that the early Venus atmosphere was more enriched in water than it is today [e.g., *Rasool and de Bergh*, 1970; *Lewis*, 1970; *Donahue et al.*, 1982] and had lost H_2O either due to a runaway greenhouse [*Ingersoll*, 1969; *Rasool and de Bergh*, 1970] or a moist greenhouse [*Kasting and Pollack*, 1983; *Kasting*, 1988] and escape processes [*Kulikov et al.*, 2006; *Lammer et al.*, 2008] or even that the water has been reinjected within the mantle [*Albarede*, 2009].

We use our predictive scaling laws to redraw Venus history and propose below different evolution scenarios (Figures 18 and 19). From the initial conditions, the surface of the planet would be molten at ERCS (even for low $[H_2O]_{t0}$: Figure 7). As MO degassing proceeds, water condensation might occur within the atmosphere and subsequent clouds formation should tend to increase planetary albedo to its current value. Assuming a x^* value allowing water condensation, Figure 18 presents Venus' relative position to the critical distance ($D^* = 1$) as a function of planetary albedo and solar constant (which is time dependent). On proto-Venus (young Sun), a water ocean can form with at least an albedo of 0.45 and 0.3 M_{EO}. For the present-day solar constant, an albedo lower than 0.6 precludes water ocean formation. At this albedo limit value of 0.6, at least 0.3 M_{EO} is required to condense (Figures 18 and 19b). With time, solar constant increases, and higher albedos are required to sustain water oceans on longer timescale (Figures 18 and 19). However, the longer it takes to form a thick cloud cover (a high albedo), the less probable it is to keep a sufficient amount of water in the atmosphere to form a water ocean because of the desiccation through escape processes. Using Venus'

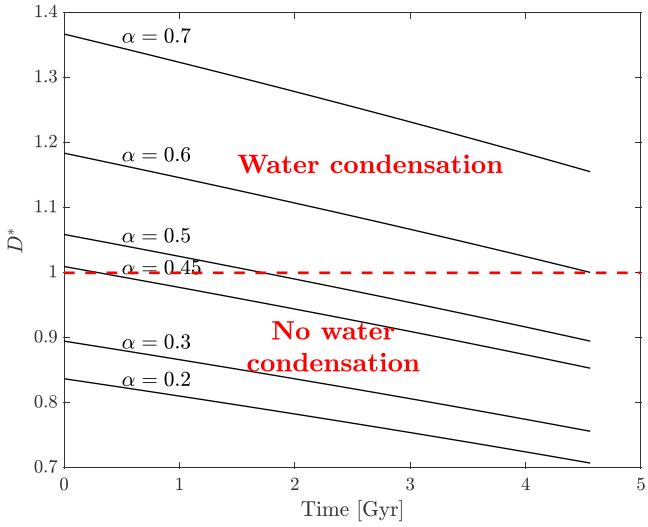


Figure 18. Water condensation diagram for different albedo and solar constant (time dependent) for Venus, using D^* (equation (13)), the present-day CO_2 content, and assuming an initial water content $[H_2O]_{t0}$ = 1 M_{EO}. Above the red dashed line ($D^* = 1$), the formation of an ocean occurs. Parameters used for the calculations are given in Table 2.

present-day albedo ($\alpha = 0.7$) and CO_2 content (90 bar), only $[H_2O]_{t0}$ = 0.143 M_{EO} (38 bar) is required to form a water ocean with the current solar constant ($x^* < 0.7$ in Figure 19b); and only $[H_2O]_{t0}$ = 0.1 M_{EO} (27 bar) for the faint young Sun ($x^* < 0.77$ in Figure 19a). Recent 3-D climate models, investigating the interplay between clouds, surface topography, and rotation, suggest that a slower rotation would further favor early water ocean formation [*Way et al.*, 2016]. If a water ocean formed during Venus history, water might have been reinjected into the mantle [*Albarede*, 2009] to explain its current dry atmosphere.

The current high albedo of Venus is linked to the thickness and the composition of its cloud cover, reflecting 70% of the incoming sunlight ($\alpha = 0.7$). Nevertheless, there is a competition between two phenomena: an important cloud cover leads to high planetary albedo, decreasing the absorbed solar flux and so the temperature. On the other hand, it impedes escape of the radiative flux to space, increasing the blanketing effect and thus surface temperatures (see section 4.2). It is then important to understand the dynamic of clouds and their repartition in the atmosphere. Neglecting their blanketing effect underestimates surface temperatures by around 140 K [*Titov et al.*, 2013]. Thus, the formation time of such a cloud cover, leading to a strong albedo, combined with the remaining water content and solar constant is critical to understand the past evolution of

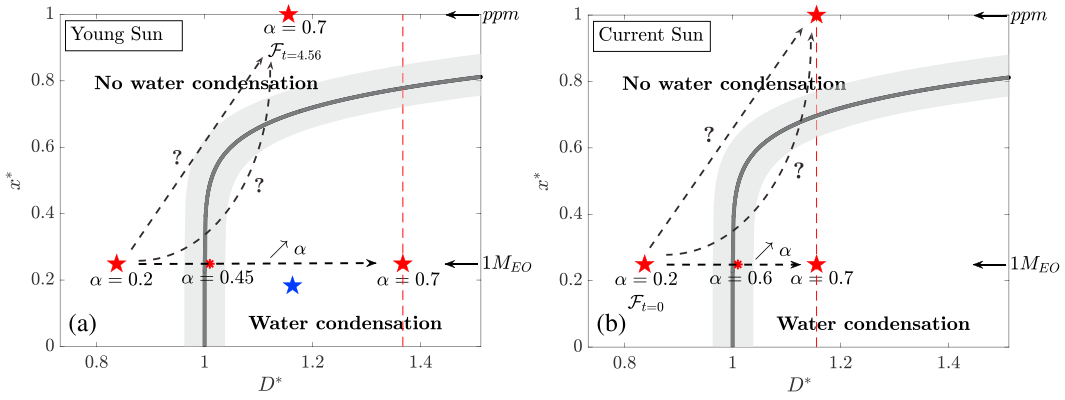


Figure 19. Venus' (red stars) possible evolutions depending on albedo and solar constant. The condensation limit in black is based on x^* and D^* (equations (11) and (13)). The red asterisks indicate the lowest albedo value that permits water condensation on Venus, for the solar constant (a) of the young Sun and (b) of the current Sun. The water content is indicated by the arrows on the right-hand side. The label "ppm" stands for low water concentration (on the order of 1 ppm or less). The vertical dashed lines indicate Venus possible locations, depending on the water content. The blue star (Figure 19a) stands for the early Earth with $[H_2O]_{t0}$ = 1 M_{EO} and $[CO_2]_{t0}$ = 60 bar. Parameters used for the calculations are given in Table 2.

Venus and its ability to condense water. Note that the rotation rate might also play an important role as it controls atmospheric circulation and spatial distribution of clouds, and thus incident energy redistribution [*Yang et al.*, 2014].

6. Conclusion

The early evolution of a rocky planet experiencing a magma ocean phase is characterized by two dynamic regimes. The first one is defined by rapid cooling through vigorous convective motions and strong degassing of the atmosphere, in opposition to the later quasi steady state, where surface temperature and heat fluxes evolve much more slowly. Surface conditions are then controlled by the balance between the absorbed solar flux (which evolves faintly compared to the convective flux from the mantle in the first stage) and the outgoing infrared flux. When the convective flux from the mantle becomes one order of magnitude lower than the absorbed solar flux, the end of the first rapid cooling stage ("ERCS") is reached. That moment is used as a reference evolution time to compare the thermodynamical state of the planet. Simulating the cooling of a magma ocean in interaction with the atmosphere shows that water condensation at ERCS strongly depends on both H_2O and CO_2 contents. The corresponding surface conditions at ERCS may give rise to three different types of planet as a function of the solar distance and the volatile content: (1) planets with a water ocean overlying a solid surface: type I (like the Earth); (2) planets with a molten surface and without water ocean: type II; and (3) planets with a solid surface without water ocean: type III.

From our calculations, we provide scaling laws to predict water condensation on an Earth-like planet at ERCS for different initial conditions, using either our grey radiative-convective model or our nongrey *k*-correlated radiative-convective model for the atmosphere. Those scaling laws are valid for a wide range of parameters such as different volatile contents, different solar distances, different planetary albedos and during all the lifetime of our solar system. Our predictions for water condensation are consistent with existing models that focus on the location of the habitable zone. However, these models postulate rather than calculate surface conditions that our model determines taking into account early interactions between the interior and the atmosphere. Furthermore, surface temperatures follow two distinct trends from either side of the critical distance. We tested our predictions in the case of Venus and have shown that water ocean formation might have occurred during Venus history depending on the history of clouds formation and on the assumed initial water content.

Appendix A: Magma Ocean's Viscosity

As shown in Figure 1, the interpolated viscosity law defined in section 2.1.2 delays both the end of rapid cooling stage and complete solidification time (time when $R_s = R_p$). Indeed, the transition to a solid-state mantle

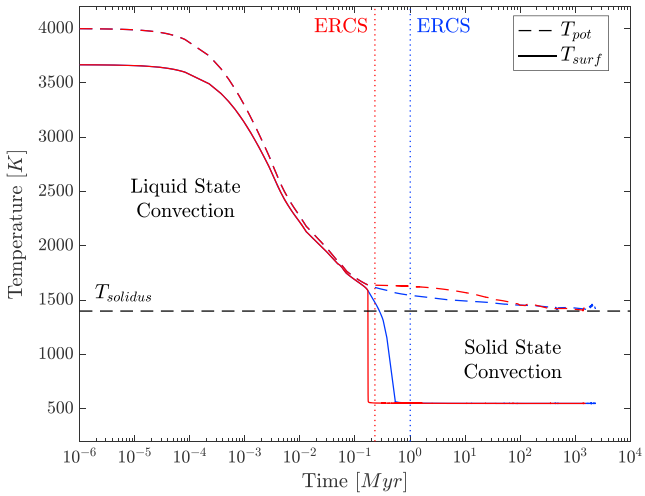


Figure A1. Thermal evolution of the magma ocean using the viscosity law from *Lebrun et al.* [2013] (red) and the analytical one presented in this study (blue). Corresponding ERCS times are indicated by the vertical dotted lines. The solid and the dashed lines stand for surface and potential temperatures, respectively. Earth-like planet, $[H_2O]_{t0}$ = 0.621 M_{EO}, $[CO_2]_{t0} = 4 \times 10^{-2}$ wt %, D = 1 AU, grey radiative-convective cloud-free atmosphere, α = 0.2, young Sun.

is shifted to a lower liquid fraction than the classic $\phi_c = 0.4$, which is reached later. Furthermore, it smoothes the rheology transition from liquid to a solid-state convection, which is more realistic and in agreement with experimental data [*Takei and Holtzman*, 2009]. Note that it does not affect the surface conditions reached at ERCS.

Appendix B: Processes Occurring During Magma Ocean Solidification

Figure 1 shows that the solidus curve is steeper than the adiabats, and therefore, a superadiabatic temperature difference ΔT_{sa} would develop in any growing solid layer of thickness $h = R_S - R_{core}$ (note that in this case ΔT_{sa} and h are proportional). This configuration is gravitationally unstable [*Solomatov*, 2015]. Figure 1 shows that a small $\Delta T_{sa} \approx 5$ K (corresponding to $h \approx 50$ km) is sufficient for the solid layer $Ra(h, \Delta T_{sa})$ to exceed the critical value $Ra_C \approx 650$ [*Chandrasekhar*, 1961] for a solid viscosity of $\eta_s = 10^{18}$ Pa s. The value of η_s in the lower mantle, which depends on creep mechanism and composition [*Hustoft et al.*, 2007; *Boioli et al.*, 2017], is still debated, but a large range of values will allow convection in the growing solid layer (Figure B1a). Its overturn time $t_C = h/U$ can be estimated using the Stokes velocity $U = 2\alpha_T \rho \Delta T_{sa} g h^2 / 9\eta_s$. It is smaller than the MO solidification time obtained considering no convection within the underlying solid layer for a large range of solid viscosities (Figure 1). Any overturn of the solid layer would reheat the bottom of the MO and therefore delay its complete solidification.

In addition, incompatible elements going preferentially in the liquid phase, solidification results in a progressive enrichment of the liquid magma in iron (and other incompatible elements) compared to the underlying solid cumulates. This would tend to build an unstable density stratification in the growing solids and further diminish their gravitational stability. Recent 2-D numerical simulations taking into account the full thermochemical effects indeed confirm that solid-state convection would develop inside the growing solid cumulates before the MO complete solidification [*Maurice et al.*, 2017].

Note that our model is built on two instantaneous and local balances for the heat fluxes and for the atmospheric volatile contents, which do not depend explicitly on time (since there is no escape of volatiles). So since the ERCS is based on a flux condition ($F_{conv} \leq 0.1 F_\odot$), the surface conditions at ERCS do not depend on the details of the MO cooling history. Indeed, the dashed lines on Figure 7, obtained by considering a secular cooling only occurring over the liquid-state mantle (i.e., between the solidification front R_S and the surface), are indistinguishable from the solid lines obtained with the secular cooling calculated over the whole mantle.

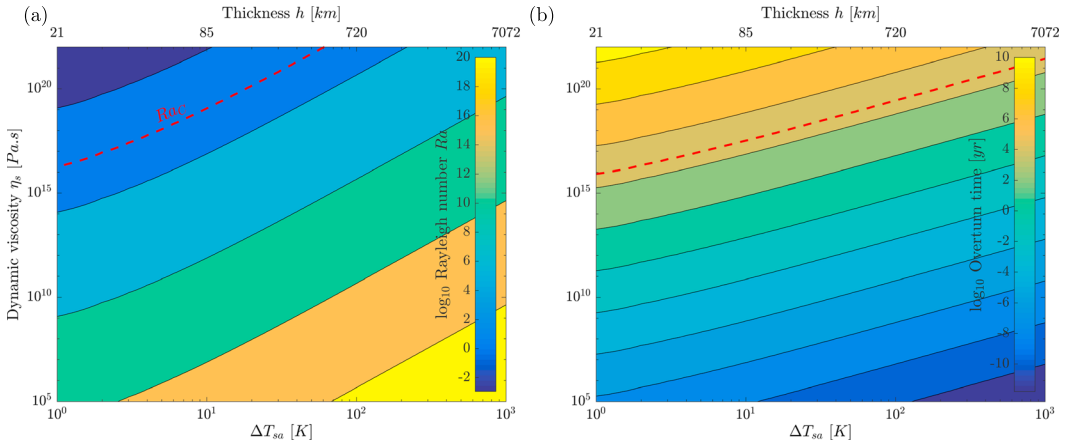


Figure B1. (a) Rayleigh number of the growing solid layer at the bottom of the mantle as a function of viscosity η_s and temperature difference ΔT_{sa}. Above Ra_C (below the red curve), the configuration is unstable and solid-state mantle convection can occur. (b) Characteristic overturning time t_C of the gravitationally unstable solid layer. The red line represents the MO solidification time considering no convection within the underlying solid layer, for a grey atmosphere, without clouds, $[H_2O]_{t0} = 0.371$ M_{EO}, $[CO_2]_{t0} = 2 \times 10^{-2}$ wt %, $D = 1$ AU. All t_C shorter than this lower limit show that convection might indeed occur within the solidifying layer before MO complete crystallization.

Appendix C: Fate of the Volatiles

Concerning the volatile mass transfer between the magma ocean and the atmosphere, we used the same parametrization as *Lebrun et al.* [2013] described hereafter.

As the magma crystallizes, the volatiles go preferentially into the residual liquid, which becomes enriched in volatiles. We assume that the degassing of these species occurs by exsolution, above the saturation limit. Then, bubbles rise up and finally burst at the surface. The upward velocity of the gas pocket (the percolation velocity) is higher than the velocity timescale of the liquid-state convection [*Lebrun et al.*, 2013]. It means that gas pieces will easily separate from the melt: volatiles reach the surface faster than the solidification front does (R_S in Figure 1b). Thus, there is a balance of the volatile content on both sides of the surface at each time step.

The volatile mass balance is given by

$$k_{\mathrm{vol}} X_{\mathrm{vol}} M_{\mathrm{solid}} + X_{\mathrm{vol}} M_{\mathrm{liquid}} + \frac{4\pi R_p^2}{g} P(X_{\mathrm{vol}}) = X_0 M_0, \tag{C1}$$

where X_0 and M_0 are respectively the initial mass fraction of volatiles and the initial mass of liquid, X_{vol} is the mass fraction of volatile dissolved in the magma, M_{solid} and M_{liquid} are the masses of solid and liquid phase and k_{vol} is the distribution coefficient for each volatile species between the solid and liquid phases. It scales as

$$k_{\mathrm{vol}} = \frac{M_{s_{\mathrm{perov}}} k_{\mathrm{vol}_{\mathrm{perov}}} + M_{s_{\mathrm{lherz}}} k_{\mathrm{vol}_{\mathrm{lherz}}}}{M_{s_{\mathrm{perov}}} + M_{s_{\mathrm{lherz}}}}, \tag{C2}$$

where $M_{s_{\mathrm{perov}}}$ and $M_{s_{\mathrm{lherz}}}$ represent respectively the masses of the solid phases for perovskite and lherzolite, $k_{\mathrm{vol}_{\mathrm{perov}}}$ and $k_{\mathrm{vol}_{\mathrm{lherz}}}$ are respectively the partition coefficients of volatile (H_2O or CO_2) for perovskite and lherzolite [*Elkins-Tanton*, 2008] (for the values refer to Table 1).

It is often assumed that the MO and the atmosphere are in equilibrium, and their volatiles partial pressures $P(X_{\mathrm{vol}})$ are given by

$$P(X_{\mathrm{H_2O}}) = \left(\frac{X_{\mathrm{H_2O}}}{6.8 \times 10^{-8}} \right)^{1/0.7}, \tag{C3}$$

$$P(X_{\mathrm{CO_2}}) = \frac{X_{\mathrm{CO_2}}}{4.4 \times 10^{-12}}. \tag{C4}$$

Acknowledgments
We acknowledge funding from the CNRS-INSU-CNES national planetology program (PNP). We thank Claude Mercier for her precious help using the IAS clusters (ERM/Univ. Paris-Sud). We gratefully acknowledge the discussions with Gianluca Gerardi and the European ITN CREEP. We thank also the Editor and two anonymous reviewers for their valuables suggestions on the manuscript. All the data presented can be downloaded at https://transfert.u-psud.fr/9s1m9. Any further queries can be directed to A. Salvador (arnaud.salvador@u-psud.fr).

References

Abe, Y. (1993), Physical state of the very early Earth, *Lithos*, *30*(3–4), 223–235, doi:10.1016/0024-4937(93)90037-D.
Abe, Y. (1997), Thermal and chemical evolution of the terrestrial magma ocean, *Phys. Earth Planet. Inter.*, *100*(1–4), 27–39, doi:10.1016/S0031-9201(96)03229-3.
Abe, Y., and T. Matsui (1985), The formation of an impact-generated H_2O atmosphere and its implications for the early thermal history of the Earth, *J. Geophys. Res.*, *90*(2), 545–559, doi:10.1029/JB090iS02p0C545.
Abe, Y., and T. Matsui (1988), Evolution of an impact-generated H_2O–CO_2 atmosphere and formation of a hot proto-ocean on Earth, *J. Atmos. Sci.*, *45*(21), 3081–3101, doi:10.1175/1520-0469(1988)045<3081:EOAIGH>2.0.CO;2.
Abe, Y., A. Abe-Ouchi, N. H. Sleep, and K. J. Zahnle (2011), Habitable zone limits for dry planets, *Astrobiology*, *11*(5), 443–460, doi:10.1089/ast.2010.0545.
Ahrens, T. J. (1993), Impact erosion of terrestrial planetary atmospheres, *Annu. Rev. Earth Planet. Sci.*, *21*, 525–55.
Albarede, F. (2009), Volatile accretion history of the terrestrial planets and dynamic implications, *Nature*, *461*(7268), 1227–1233.
Andrault, D., N. Bolfan-Casanova, G. L. Nigro, M. A. Bouhifd, G. Garbarino, and M. Mezouar (2011), Solidus and liquidus profiles of chondritic mantle: Implication for melting of the Earth across its history, *Earth Planet. Sci. Lett.*, *304*(1–2), 251–259, doi:10.1016/j.epsl.2011.02.006.
Andrault, D., S. Petitgirard, G. Lo Nigro, J.-L. Devidal, G. Veronesi, G. Garbarino, and M. Mezouar (2012), Solid-liquid iron partitioning in Earth's deep mantle, *Nature*, *487*(7407), 354–357.
Andrault, D., G. Pesce, M. A. Bouhifd, N. Bolfan-Casanova, J.-M. Hénot, and M. Mezouar (2014), Melting of subducted basalt at the core-mantle boundary, *Science*, *344*(6186), 892–895, doi:10.1126/science.1250466.
Bahcall, J. N., M. H. Pinsonneault, and S. Basu (2001), Solar models: Current epoch and time dependences, neutrinos, and helioseismological properties, *Astrophys. J.*, *555*(2), 990–1012.
Boioli, F., P. Carrez, P. Cordier, B. Devincre, K. Gouriet, P. Hirel, A. Kraych, and S. Ritterbex (2017), Pure climb creep mechanism drives flow in Earth's lower mantle, *Sci. Adv.*, *3*(3), e1601958, doi:10.1126/sciadv.1601958.
Boukaré, C. E., Y. Ricard, and G. Fiquet (2015), Thermodynamics of the MgO-FeO-SiO_2 system up to 140 GPa: Application to the crystallization of Earth's magma ocean, *J. Geophys. Res. Solid Earth*, *120*, 6085–6101, doi:10.1002/2015JB011929.
Cameron, A. G. W. (1983), Origin of the atmospheres of the terrestrial planets, *Icarus*, *56*(2), 195–201, doi:10.1016/0019-1035(83)90032-5.
Canup, R. M. (2008), Accretion of the Earth, *Philos. Trans. R. Soc. A*, *366*(1883), 4061–4075.
Cartigny, P., F. Pineau, C. Aubaud, and M. Javoy (2008), Towards a consistent mantle carbon flux estimate: Insights from volatile systematics (H_2O/Ce, δD, CO_2/Nb) in the North Atlantic mantle (14°N and 34°N), *Earth Planet. Sci. Lett.*, *265*(3–4), 672–685, doi:10.1016/j.epsl.2007.11.011.

Chandrasekhar, S. (1961), *Hydrodynamic and Hydromagnetic Stability, Int. Ser. of Monogr. on Phys.*, Clarendon, Oxford, U. K.
de Bergh, C., B. Bézard, D. Crisp, J. Maillard, T. Owen, J. Pollack, and D. Grinspoon (1995), Water in the deep atmosphere of Venus from high-resolution spectra of the night side, *Adv. Space Res.*, *15*(4), 79–88, doi:10.1016/0273-1177(94)00067-B.
de Bergh, C., V. Moroz, F. Taylor, D. Crisp, B. Bézard, and L. Zasova (2006), The composition of the atmosphere of Venus below 100 km altitude: An overview, *Planet. Space Sci*, *54*(13–14), 1389–1397, doi:10.1016/j.pss.2006.04.020.
Donahue, T. M., J. H. Hoffman, R. R. Hodges, and A. J. Watson (1982), Venus was wet: A measurement of the ratio of deuterium to hydrogen, *Science*, *216*(4546), 630–633, doi:10.1126/science.216.4546.630.
Elkins-Tanton, L. T. (2008), Linked magma ocean solidification and atmospheric growth for Earth and Mars, *Earth Planet. Sci. Lett.*, *271*(1–4), 181–191, doi:10.1016/j.epsl.2008.03.062.
Elkins-Tanton, L. T. (2011), Formation of early water oceans on rocky planets, *Astrophys. Space Sci.*, *332*(2), 359–364, doi:10.1007/s10509-010-0535-3.
Elkins-Tanton, L. T. (2012), Magma oceans in the inner solar system, *Annu. Rev. Earth Planet. Sci.*, *40*, 113–139, doi:10.1146/annurev-earth-042711-105503.
Eymet, V., C. Coustet, and B. Piaud (2016), Kspectrum: An open-source code for high-resolution molecular absorption spectra production, *J. Phys. Conf. Ser.*, *676*(1), 012005.
Ezer, D., and A. G. W. Cameron (1965), A study of solar evolution, *Can. J. Phys.*, *43*(8), 1497–1517, doi:10.1139/p65-140.
Fiquet, G., A. L. Auzende, J. Siebert, A. Corgne, H. Bureau, H. Ozawa, and G. Garbarino (2010), Melting of peridotite to 140 gigapascals, *Science*, *329*(5998), 1516–1518, doi:10.1126/science.1192448.
Foley, B. J., and P. E. Driscoll (2016), Whole planet coupling between climate, mantle, and core: Implications for rocky planet evolution, *Geochem. Geophys. Geosyst.*, *17*, 1885–1914, doi:10.1002/2015GC006210.
Foley, B. J., D. Bercovici, and L. T. Elkins-Tanton (2014), Initiation of plate tectonics from post-magma ocean thermochemical convection, *J. Geophys. Res. Solid Earth*, *119*, 8538–8561, doi:10.1002/2014JB011121.
Gillmann, C., and P. Tackley (2014), Atmosphere/mantle coupling and feedbacks on Venus, *J. Geophys. Res. Planets*, *119*, 1189–1217, doi:10.1002/2013JE004505.
Gillmann, C., G. J. Golabek, and P. J. Tackley (2016), Effect of a single large impact on the coupled atmosphere-interior evolution of Venus, *Icarus*, *268*, 295–312, doi:10.1016/j.icarus.2015.12.024.
Gough, D. O. (1981), Solar interior structure and luminosity variations, *Sol. Phys.*, *74*(1), 21–34, doi:10.1007/BF00151270.
Hamano, K., Y. Abe, and H. Genda (2013), Emergence of two types of terrestrial planet on solidification of magma ocean, *Nature*, *497*(7451), 607–610.
Hamano, K., H. Kawahara, Y. Abe, M. Onishi, and G. L. Hashimoto (2015), Lifetime and spectral evolution of a magma ocean with a steam atmosphere: Its detectability by future direct imaging, *Astrophys. J.*, *806*(2), 216, doi:10.1088/0004-637X/806/2/216.
Hart, M. H. (1979), Habitable zones about main sequence stars, *Icarus*, *37*(1), 351–357, doi:10.1016/0019-1035(79)90141-6.
Hashimoto, G. L., Y. Abe, and S. Sugita (2007), The chemical composition of the early terrestrial atmosphere: Formation of a reducing atmosphere from CI-like material, *J. Geophys. Res.*, *112*, E05010, doi:10.1029/2006JE002844.
Helo, C., M.-A. Longpre, N. Shimizu, D. A. Clague, and J. Stix (2011), Explosive eruptions at mid-ocean ridges driven by CO_2-rich magmas, *Nat. Geosci.*, *4*(4), 260–263.
Holland, H. D. (1962), Model for the evolution of the Earth's atmosphere, in *Petrologic Studies: A Volume to Honor A. F. Buddington*, edited by A. E. J. Engel, H. L. James, and B. F. Leonard, pp. 447–477, Geol. Soc. of Am., New York.
Holland, H. D. (1978), *The Chemistry of the Atmosphere and Oceans*, Wiley, New York.
Hostetler, C. J., and M. J. Drake (1980), On the early global melting of the terrestrial planets, *Lunar Planet. Sci. Conf. Proc.*, *11*, 1915–1929.
Hustoft, J., T. Scott, and D. L. Kohlstedt (2007), Effect of metallic melt on the viscosity of peridotite, *Earth Planet. Sci. Lett.*, *260*(1–2), 355–360, doi:10.1016/j.epsl.2007.06.011.
Ikoma, M., and H. Genda (2006), Constraints on the mass of a habitable planet with water of nebular origin, *Astrophys. J.*, *648*(1), 696–706, doi:10.1086/505780.
Ingersoll, A. P. (1969), The runaway greenhouse: A history of water on Venus, *J. Atmos. Sci.*, *26*(6), 1191–1198.
Jaupart, C., and J.-C. Mareschal (2011), *Heat Generation and Transport in the Earth*, Cambridge Univ. Press, Cambridge, U. K.
Karato, S.-I., and P. Wu (1993), Rheology of the upper mantle: A synthesis, *Science*, *260*(5109), 771–778, doi:10.1126/science.260.5109.771.
Karki, B. B., and L. P. Stixrude (2010), Viscosity of $MgSiO_3$ liquid at Earth's mantle conditions: Implications for an early magma ocean, *Science*, *328*(5979), 740–742, doi:10.1126/science.1188327.
Kasting, J. F. (1988), Runaway and moist greenhouse atmospheres and the evolution of Earth and Venus, *Icarus*, *74*(3), 472–494, doi:10.1016/0019-1035(88)90116-9.
Kasting, J. F. (1991), CO_2 condensation and the climate of early Mars, *Icarus*, *94*(1), 1–13, doi:10.1016/0019-1035(91)90137-I.
Kasting, J. F., and J. B. Pollack (1983), Loss of water from Venus. I. Hydrodynamic escape of hydrogen, *Icarus*, *53*(3), 479–508, doi:10.1016/0019-1035(83)90212-9.
Kasting, J. F., D. P. Whitmire, and R. T. Reynolds (1993), Habitable zones around main sequence stars, *Icarus*, *101*(1), 108–128, doi:10.1006/icar.1993.1010.
Kelemen, P. B., G. Hirth, N. Shimizu, M. Spiegelman, and H. J. Dick (1997), A review of melt migration processes in the adiabatically upwelling mantle beneath oceanic spreading ridges, *Philos. Trans. R. Soc. A*, *355*(1723), 283–318, doi:10.1098/rsta.1997.0010.
Kopparapu, R. K. (2013), A revised estimate of the occurrence rate of terrestrial planets in the habitable zones around Kepler M-dwarfs, *Astrophys. J. Lett.*, *767*(1), L8.
Kopparapu, R. K., E. T. Wolf, J. Haqq-Misra, J. Yang, J. F. Kasting, V. Meadows, R. Terrien, and S. Mahadevan (2016), The inner edge of the habitable zone for synchronously rotating planets around low-mass stars using general circulation models, *Astrophys. J.*, *819*(1), 84.
Kopparapu, R. K., R. Ramirez, J. F. Kasting, V. Eymet, T. D. Robinson, S. Mahadevan, R. C. Terrien, S. Domagal-Goldman, V. Meadows, and R. Deshpande (2013), Habitable zones around main-sequence stars: New estimates, *Astrophys. J.*, *770*(1), 82, doi:10.1088/0004-637X/770/1/82.
Kopparapu, R. K., R. M. Ramirez, J. SchottelKotte, J. F. Kasting, S. Domagal-Goldman, and V. Eymet (2014), Habitable zones around main-sequence stars: Dependence on planetary mass, *Astrophys. J. Lett.*, *787*(2), L29, doi:10.1088/2041-8205/787/2/L29.
Kulikov, Y., et al. (2006), Atmospheric and water loss from early Venus, *Planet. Space Sci.*, *54*(13–14), 1425–1444, doi:10.1016/j.pss.2006.04.021.
Labrosse, S., J. W. Hernlund, and N. Coltice (2007), A crystallizing dense magma ocean at the base of the Earth's mantle, *Nature*, *450*(7171), 866–869.
Lammer, H., J. F. Kasting, E. Chassefière, R. E. Johnson, Y. N. Kulikov, and F. Tian (2008), Atmospheric escape and evolution of terrestrial planets and satellites, *Space Sci. Rev.*, *139*(1), 399–436, doi:10.1007/s11214-008-9413-5.

Lammer, H., et al. (2009), What makes a planet habitable?, *Astron. Astrophys. Rev.*, *17*(2), 181–249, doi:10.1007/s00159-009-0019-z.
Lammer, H., A. Stoekl, N. V. Erkaev, E. A. Dorfi, P. Odert, M. Guedel, Y. N. Kulikov, K. G. Kislyakova, and M. Leitzinger (2014), Origin and loss of nebula-captured hydrogen envelopes from 'sub'- to 'super-Earths' in the habitable zone of Sun-like stars, *Mon. Not. R. Astron. Soc.*, *439*(4), 3225–3238, doi:10.1093/mnras/stu085.
Lebrun, T., H. Massol, E. Chassefière, A. Davaille, E. Marcq, P. Sarda, F. Leblanc, and G. Brandeis (2013), Thermal evolution of an early magma ocean in interaction with the atmosphere, *J. Geophys. Res. Planets*, *118*, 1155–1176, doi:10.1002/jgre.20068.
Lewis, J. S. (1970), Venus: Atmospheric and lithospheric composition, *Earth Planet. Sci. Lett.*, *10*(1), 73–80, doi:10.1016/0012-821X(70)90066-X.
Maas, C., and U. Hansen (2015), Effects of Earth's rotation on the early differentiation of a terrestrial magma ocean, *J. Geophys. Res. Solid Earth*, *120*, 7508–7525, doi:10.1002/2015JB012053.
Marcq, E. (2012), A simple 1-D radiative-convective atmospheric model designed for integration into coupled models of magma ocean planets, *J. Geophys. Res.*, *117*, E01001, doi:10.1029/2011JE003912.
Marcq, E., A. Salvador, H. Massol, and A. Davaille (2017), Thermal radiation of magma ocean planets using a 1D radiative-convective model of H_2O-CO_2 atmospheres, *J. Geophys. Res. Planets*, *122*, doi:10.1002/2016JE005224.
Marty, B. (2012), The origins and concentrations of water, carbon, nitrogen and noble gases on Earth, *Earth Planet. Sci. Lett.*, *313–314*, 56–66, doi:10.1016/j.epsl.2011.10.040.
Massol, H., et al. (2016), Formation and evolution of protoatmospheres, *Space Sci. Rev.*, *205*, 153–211, doi:10.1007/s11214-016-0280-1.
Matsui, T., and Y. Abe (1984), The formation of an impact-generated H_2O atmosphere and its implications for the early thermal history of the Earth, *Proc. Lunar Planet. Sci. Conf. 15th, Part 2, J. Geophys. Res.*, *90*, C517–C518.
Matsui, T., and Y. Abe (1986), Formation of a "magma ocean" on the terrestrial planets due to the blanketing effect of an impact-induced atmosphere, *Earth Moon Planets*, *34*(3), 223–230, doi:10.1007/BF00145081.
Maurice, M., N. Tosi, H. Samuel, A.-C. Plesa, C. Hüttig, and D. Breuer (2017), Onset of solid-state mantle convection and mixing during magma ocean solidification, *J. Geophys. Res. Planets*, *122*, 577–598, doi:10.1002/2016JE005250.
Mei, S., W. Bai, T. Hiraga, and D. Kohlstedt (2002), Influence of melt on the creep behavior of olivine–basalt aggregates under hydrous conditions, *Earth Planet. Sci. Lett.*, *201*(3–4), 491–507, doi:10.1016/S0012-821X(02)00745-8.
Moeller, A., and U. Hansen (2013), Influence of rotation on the metal rain in a Hadean magma ocean, *Geochem. Geophys. Geosyst.*, *14*, 1226–1244, doi:10.1002/ggge.20087.
Morbidelli, A., J. Chambers, J. I. Lunine, J. M. Petit, F. Robert, G. B. Valsecchi, and K. E. Cyr (2000), Source regions and timescales for the delivery of water to the Earth, *Meteorit. Planet. Sci.*, *35*(6), 1309–1320, doi:10.1111/j.1945-5100.2000.tb01518.x.
Morbidelli, A., J. I. Lunine, D. P. O'Brien, S. N. Raymond, and K. J. Walsh (2012), Building terrestrial planets, *Annu. Rev. Earth Planet. Sci.*, *40*, 251–275, doi:10.1146/annurev-earth-042711-105319.
Nakajima, S., Y.-Y. Hayashi, and Y. Abe (1992), A study on the "runaway greenhouse effect" with a one-dimensional radiative–convective equilibrium model, *J. Atmos. Sci.*, *49*(23), 2256–2266, doi:10.1175/1520-0469(1992)049<2256:ASOTGE>2.0.CO;2.
Nomura, R., H. Ozawa, S. Tateno, K. Hirose, J. Hernlund, S. Muto, H. Ishii, and N. Hiraoka (2011), Spin crossover and iron-rich silicate melt in the Earth's deep mantle, *Nature*, *473*(7346), 199–202.
O'Brien, D. P., A. Morbidelli, and H. F. Levison (2006), Terrestrial planet formation with strong dynamical friction, *Icarus*, *184*(1), 39–58, doi:10.1016/j.icarus.2006.04.005.
O'Brien, D. P., K. J. Walsh, A. Morbidelli, S. N. Raymond, and A. M. Mandell (2014), Water delivery and giant impacts in the "Grand Tack" scenario, *Icarus*, *239*, 74–84.
Pineau, F., and M. Javoy (1994), Strong degassing at ridge crests: The behaviour of dissolved carbon and water in basalt glasses at 14°N, Mid-Atlantic Ridge, *Earth Planet. Sci. Lett.*, *123*(1), 179–198, doi:10.1016/0012-821X(94)90266-6.
Poldervaart, A. (1955), Chemistry of the Earth's crust, *Geol. Soc. Am. Spec. Pap.*, *62*, 119–144.
Rasool, S. I., and C. de Bergh (1970), The runaway greenhouse and the accumulation of CO_2 in the Venus atmosphere, *Nature*, *226*(5250), 1037–1039.
Raymond, S. N., T. Quinn, and J. I. Lunine (2007), High-resolution simulations of the final assembly of Earth-Like Planets. 2. Water delivery and planetary habitability, *Astrobiology*, *7*(1), 66–84, doi:10.1089/ast.2006.06-0126.
Ronov, A. B., and A. A. Yaroshevsky (1969), Chemical composition of the Earth's crust, in *The Earth's Crust and Upper Mantle*, edited by P. J. Hart, pp. 37–57, AGU, Washington, D. C.
Roscoe, R. (1952), The viscosity of suspensions of rigid spheres, *Br. J. Appl. Phys.*, *3*(8), 267–269.
Rubey, W. W. (1951), Geologic history of sea water: An attempt to state the problem, *Geol. Soc. Am. Bull.*, *62*(9), 1111–1148.
Safronov, V. (1978), The heating of the Earth during its formation, *Icarus*, *33*(1), 3–12, doi:10.1016/0019-1035(78)90019-2.
Sarda, P., and D. Graham (1990), Mid-ocean ridge popping rocks: Implications for degassing at ridge crests, *Earth Planet. Sci. Lett.*, *97*(3), 268–289, doi:10.1016/0012-821X(90)90047-2.
Schaefer, L., and B. J. Fegley (2010), Chemistry of atmospheres formed during accretion of the Earth and other terrestrial planets, *Icarus*, *208*(1), 438–448, doi:10.1016/j.icarus.2010.01.026.
Selsis, F., J. F. Kating, B. Levrard, J. Paillet, I. Ribas, and X. Delfosse (2007), Habitable planets around the star Gliese 581?, *Astron. Astrophys.*, *476*(3), 1373–1387, doi:10.1051/0004-6361:20078091.
Siggia, E. D. (1994), High Rayleigh number convection, *Annu. Rev. Fluid Mech.*, *26*, 137–168.
Solomatov, V. S. (2000), Fluid dynamics of a terrestrial magma Ocean, in *Origin of the Earth and Moon*, edited by R. Canup and K. Righter, pp. 323–338, Univ. of Arizona Press, Tucson, Ariz.
Solomatov, V. S. (2007), Magma oceans and primordial mantle differentiation, in *Treatise on Geophysics*, edited by G. Schubert, chap. 9.04, pp. 91–119, Elsevier, Amsterdam.
Solomatov, V. S. (2015), Magma oceans and primordial mantle differentiation, in *Treatise on Geophysics (Second Edition)*, 2nd ed., edited by G. Schubert, chap. 9.04, pp. 81–104, Elsevier, Oxford, U. K.
Stamnes, K., S.-C. Tsay, W. Wiscombe, and K. Jayaweera (1988), Numerically stable algorithm for discrete-ordinate-method radiative transfer in multiple scattering and emitting layered media, *Appl. Opt.*, *27*(12), 2502–2509, doi:10.1364/AO.27.002502.
Stixrude, L., N. de Koker, N. Sun, M. Mookherjee, and B. B. Karki (2009), Thermodynamics of silicate liquids in the deep Earth, *Earth Planet. Sci. Lett.*, *278*(3–4), 226–232, doi:10.1016/j.epsl.2008.12.006.
Takei, Y., and B. K. Holtzman (2009), Viscous constitutive relations of solid-liquid composites in terms of grain boundary contiguity: 1. Grain boundary diffusion control model, *J. Geophys. Res.*, *114*, B06205, doi:10.1029/2008JB005850.
Tateno, S., K. Hirose, and Y. Ohishi (2014), Melting experiments on peridotite to lowermost mantle conditions, *J. Geophys. Res. Solid Earth*, *119*, 4684–4694, doi:10.1002/2013JB010616.
Titov, D. V., G. Piccioni, P. Drossart, and W. J. Markiewicz (2013), *Radiative Energy Balance in the Venus Atmosphere*, 23–53, Springer, New York.

Tonks, W. B., and H. J. Melosh (1993), Magma ocean formation due to giant impacts, *J. Geophys. Res.: Planets*, *98*(E3), 5319–5333, doi:10.1029/92JE02726.

Walker, J. C. (1986), Impact erosion of planetary atmospheres, *Icarus*, *68*(1), 87–98, doi:10.1016/0019-1035(86)90076-X.

Watkins, J. G. H. (1983), The consequences of cometary and asteroidal impacts on the volatile inventories of the terrestrial planets, PhD thesis, Massachusetts Inst. of Technol., Cambridge, Mass.

Way, M. J., A. D. Del Genio, N. Y. Kiang, L. E. Sohl, D. H. Grinspoon, I. Aleinov, M. Kelley, and T. Clune (2016), Was Venus the first habitable world of our solar system?, *Geophys. Res. Lett.*, *43*, 8376–8383, doi:10.1002/2016GL069790.

Wood, J. A., J. S. Dickey Jr., U. B. Marvin, and B. N. Powell (1970), Lunar anorthosites and a geophysical model of the Moon, in *Geochimica et Cosmochimica Acta Supplement, Proceeding of the Apollo 11 Lunar Science Conference, Houston, Texas, 5–8 Jan.*, vol. 1, edited by A. A. Levinson, pp. 965–988, Pergammon Press, New York.

Yang, J., G. Boué, D. C. Fabrycky, and D. S. Abbot (2014), Strong dependence of the inner edge of the habitable zone on planetary rotation rate, *Astrophys. J. Lett.*, *787*(1), L2, doi:10.1088/2041-8205/787/1/L2.

Zahnle, K., N. Arndt, C. Cockell, A. Halliday, E. Nisbet, F. Selsis, and N. H. Sleep (2007), Emergence of a habitable planet, in *Geology and Habitability of Terrestrial Planets*, edited by K. E. Fishbaugh et al., pp. 35–78, Springer, New York, doi:10.1007/978-0-387-74288-5_3.